Geophysical Journal International

Geophys. J. Int. (2023) **235,** 1959–1981
Advance Access publication 2023 August 18
GJI Seismology

https://doi.org/10.1093/gji/ggad323

Comparison of force and moment tensor estimations of subevents during the 2022 Hunga–Tonga submarine volcanic eruption

J. Thurin and C. Tape

Geophysical Institute, University of Alaska Fairbanks, Fairbanks, 99775, Alaska, USA E-mail: jthurin@alaska.edu

Accepted 2023 August 7. Received 2023 August 5; in original form 2022 October 28

SUMMARY

The 2022 January 15 Hunga–Tonga submarine volcanic eruption was unprecedented in the modern era for its size, in terms of its plume height and atmospheric waves, including sound. Global seismic stations recorded maximal radiated energy during 30 min of the plume-forming phase of the eruption (04:00 to 04:30 UTC), with the largest subevents occurring over a 5-min interval starting at 04:15:17 UTC. Here, we consider two simple point-source models—force and moment tensor—and separately consider the single main subevent and the sequence of four subevents. Estimation of source models for the first subevent in the sequence is achieved with a complete search of model parameter space to find the global minimum of a waveform misfit function (body or surface waves). We performed 25 runs to explore the impact of depth, source model (force or moment tensor), wave type (body or surface), and component (vertical, radial, and transverse) on the waveform fits and estimated best-fitting source. Visualization of the misfit function reveals complex trade-offs among model parameters, highlighting the importance of characterizing uncertainties and parameter trade-offs. The four-subevent source model has up to 28 model parameters and requires an efficient search algorithm to find the best-fitting source. For this, we use the covariance matrix adaptation evolution strategy implemented on a high-performance computing cluster. The 10 four-subevent runs for each source model return sequences of subvertical downward forces and explosive-like moment tensors for each subevent. Our results show that these two simple source models provide comparable fits to regional and global seismic waveforms and that the source types for each subevent—either force direction or moment tensor source type on the eigenvalue lune—are similar enough to each other to consider that the subevents originate from the same process. Our estimation of the source mechanisms, sizes, and relative timing should benefit a physical interpretation of the eruption sequence.

Key words: Inverse theory; Earthquake source observations; Volcano seismology, Pacific Ocean.

1 INTRODUCTION

The 2022 January 15 Hunga Tonga–Hunga Ha'apai (HTHH) submarine volcanic eruption in the southwest Pacific Ocean was seen from space (Carr *et al.* 2022), heard from Alaska (Matoza *et al.* 2022), generated global atmospheric and tsunami waves (Amores *et al.* 2022; Omira *et al.* 2022), and left an indelible mark on the seafloor (Pakoksung *et al.* 2022), splitting HTHH island in half. The main eruption phase started at about 04:00 UTC and lasted several hours (Matoza *et al.* 2022), with plume formation and maximal seismic radiation occurring during the first 30 min (Proud *et al.* 2022). Globally recorded seismic waves—both regional surface and teleseismic *P* waves—reveal numerous subevents, with *P*-wave backprojection analysis identifying 14 explosive subevents spanning 30 min (Tarumi & Yoshizawa 2023). Several of these subevents have magnitudes greater than 5, with a cumulative magnitude of 6.3 assigned to four subevents spanning 270 s (Thurin *et al.* 2022).

A comprehensive analysis of the HTHH eruption requires a breadth of observations as well as sophisticated modelling analyses. Observations include the spatiotemporal data defining the plume, the seismic wavefield, the atmospheric wavefield (infrasound and pressure), the tsunami wavefield, the geochemistry of the eruptive materials (gas, ash, and rocks), and bathymetric changes of the seafloor. In addition, these observations can be examined within the broader context of the Pacific plate subduction (including sediments and fluids) beneath the Tonga plate, with rapid back-arc spreading with the Australia plate (Jarrard 1986, 2003; Bird 2003).

Our focus is on estimating the seismic source of the HTHH eruption using globally recorded seismic waves. We are motivated by the importance of estimating the timing, magnitudes, and mechanisms of subevents recorded during the eruption. Early analysis of the teleseismic *P* waves identified four primary subevents by stacking waveforms (Yuen *et al.* 2022). That study, as well as others (Table 1), found that a downward-pointing force provided good fits to seismic waves and offered a physically reasonable model for the eruption signal.

In Thurin *et al.* (2022), we formally estimated a single source mechanism common to all four subevents. In this study, we perform a more expansive analysis of the main subevent, and we expand the space of model parameters to consider separate mechanisms, magnitudes, and onset times for the four subevents. The larger number of unknown model parameters necessitates an efficient algorithm to search model parameter space. For this, we adopt the covariance matrix adaption evolution strategy (CMA-ES) introduced by Hansen & Ostermeier (2001).

In a volcanic setting such as Hunga–Tonga, and especially during an eruption, one could realistically expect a wide range of source mechanisms (Chouet 1996; Tameguri *et al.* 2002; Chouet *et al.* 2003), such as reaction forces, earthquake faulting (double-couple moment tensor), tensional or compressional cracks, explosions, implosions, and everything in between. Furthermore, the time histories accompanying these mechanisms can be long and complex. Our analysis shows that each of the four subevents within the HTHH eruptive sequence can be characterized either by a series of downward-pointing forces or a series of moment tensors having all-positive eigenvalues, representing an explosive component. Our results allow us to exclude several possible source types, which should help guide an interpretation of the physical processes associated with the HTHH eruption.

2 DATA

Our previous work on the HTHH seismic signal focused on estimating a moment tensor using regional surface waves. Here, we consider both point force and moment-tensor source models on both regional and teleseismic data sets. We gathered a data set of publicly available three-component broad-band seismograms from a total of 580 stations. Of these, 18 stations located within a 3000 km radius of the hypocentre (longitude −175.390° and latitude −20.546°) were used for the regional surface wave analysis. Fig. 2 shows a record section of vertical- and transverse-component waveforms filtered between 25–70 s, which we interpret as Rayleigh and Love waves.

Out of the remaining 562 teleseismic stations, we retained 142 stations to perform the teleseismic body-wave analysis. These stations were selected based on azimuth and distance clustering to ensure a balanced distribution within distances between 5700 and 10 900 km (Fig. 1). The time interval considered in our analysis spans from 400 s before to 3000 s after the USGS origin time (2022-01-15 04:14:45 UTC). We used ObsPy (Beyreuther *et al.* 2010; Krischer *et al.* 2015) to remove the instrument response and rotate horizontal components into radial and transverse directions.

We bandpass filtered the three-component regional waveforms between 25–70 s and the teleseismic waveforms between 15–40 s, then downsampled them to 5 samples per second to speed up calculations. All filters used in this study are causal (one-pass).

The regional station coverage of the HTHH event (Fig. 1a) is sparse, considering the objective to constrain the source type reliably (be it a full moment tensor or a point force). This motivates the complete exploration of model parameter space, as well as visualization and quantification of model parameter uncertainties.

3 ORIGIN TIME, TIME-SHIFTS, AND TRIAL SOLUTIONS

A fundamental challenge in analysing the source of the seismic signal during the HTHH eruption is the lack of short-period *P* waves. This poses challenges for identifying first-motion polarities and the event origin time, both of which can be critical for determining the source type of a seismic event. In the context of the HTHH eruption, where the source has been inferred to be axially symmetric (Yuen *et al.* 2022), having access to polarity information would help eliminate certain source types based on the sign of the first arrivals, such as explosion/implosion or upward/downward force. A downward point force source would produce positive (upward) first arrivals on seismograms, while an upward point force source would produce negative (downward) first arrivals. Similarly, an explosion radiating energy outward would generate positive first arrivals, and an implosion radiating energy inward would produce a negative first motion across the network of stations.

In our case, the lack of an accurate determination of the origin time down to a precision of less than 10 s exacerbates the source type ambiguity. For instance, reversing the direction of a downward force and applying a time-shift of half a period to its synthetic seismograms can lead to comparable waveform fits with respect to the original force, making it difficult to differentiate between source types. This is illustrated in Fig. 3, where imposing the opposite source orientation (Figs 3a and b) or type (Figs 3c and d) results in synthetics shifted by half a period, producing what is commonly referred to as a cycle-skipping, which allows accommodating the reversed polarity signal. Cycle-skipping is known to cause local minima in the misfit space in inverse problems based on least-squares measures of waveform observations.

In the following section, we consider two point-source models: a force and a moment tensor. The point force model of Kanamori & Given (1982) has been adopted for several subsequent studies of volcanic explosions (Burger & Langston 1985; Takeo 1990; Nishimura & Hamaguchi 1993; Ohminato *et al.* 2006), including the HTHH eruption (Poli & Shapiro 2022; Garza-Girón *et al.* 2023; Tarumi & Yoshizawa 2023; Zheng *et al.* 2023). The force model is based on formulating the source of seismic energy as a downward reaction force counteracting volcanic jetting. The downward point force then represents the reaction to the mass discharge from the solid-earth system into the atmosphere.

By comparison, moment tensor sources have also been used to model seismogenic volcanic events (Uhira & Takeo 1994; Legrand *et al.* 2000; Tameguri *et al.* 2002; Chouet *et al.* 2003) and shallow explosive sources (Ford *et al.* 2012; Chiang *et al.* 2014, 2016; Alvizuri *et al.* 2018; Walter & Wen 2018), prompting us to consider them as a candidate. In the context of the HTHH eruption, we will investigate the potential of both models to explain the observed seismic data. We will focus on the force and moment tensor models separately, though there are motivating reasons to consider them simultaneously (Garza-Girón *et al.* 2023), as done by Chouet *et al.* (2003) for eruptions at Stromboli in 1997. Note that the point-force model for a volcanic eruption originates from a conceptual representation where the downward reaction force emerges from the combined contribution of an instantaneous force and an implosion within an idealized cylindrical sealed chamber (Kanamori *et al.* 1984, appendix A).

Table 1. Tabular comparison of assumed and inferred source model and source time functions, in recently published studies on the HTHH seismic sequence. Here, 'estimate' refers to formally estimating parameters from observed data (and synthetic). 'Trial' refers to author's choice of parameter *a priori* rather than by estimation. PS22 = Poli & Shapiro (2022), Y22 = Yuen *et al.* (2022), T22 = Thurin *et al.* (2022), G23 = Garza-Girón *et al.* (2023), TY23 = Tarumi & Yoshizawa (2023), Z23 = Zheng *et al.* (2023), and TT23 = this study. *Z* = vertical, *R* = radial, *T* = transverse, and MT = moment tensor.

	PS22	Y22	T22	G23	TY23	Z23	TT23
Trial force (D = down and U = up)	D	D	–	D	–	D, U	D, U
Trial MT (E = explosion, I = implosion)	–	–	–	I	–	I	E, I
Estimate force direction	–	–	–	–	–	–	Y
Estimate MT (beachball pattern + orientation)	–	–	Y	–	–	–	Y
Estimate depth	–	–	Y	–	–	–	Y
Estimate or list magnitude (M_w or $\|f\|$)	Y	–	Y	Y	–	Y	Y
Teleseismic *P* waves, *Z* component	–	Y	Y	Y	Y	Y	Y
Teleseismic *P* waves, *R* component	–	–	–	–	–	Y	Y
Teleseismic *S* waves	–	–	–	–	–	Y	–
Regional surface waves, *Z* component	–	–	Y	Y	Y	Y	Y
Regional surface waves, *R* component	–	–	Y	Y	–	Y	Y
Regional surface waves, *T* component	–	–	Y	–	–	Y	Y
Global surface waves, *Z* component	Y	–	–	–	–	Y	–
Jointly estimate subevent force parameters and onset times	–	–	–	–	–	–	Y
Jointly estimate subevent MT parameters and onset times	–	–	–	–	–	–	Y
Estimate source time function	–	–	Y	Y	Y	Y	Y
Analysed number of subevents during target 5-min time interval	–	4	4	–	3	4	4
Interpreted number of sub-subevents	–	1	1	–	1	4	1

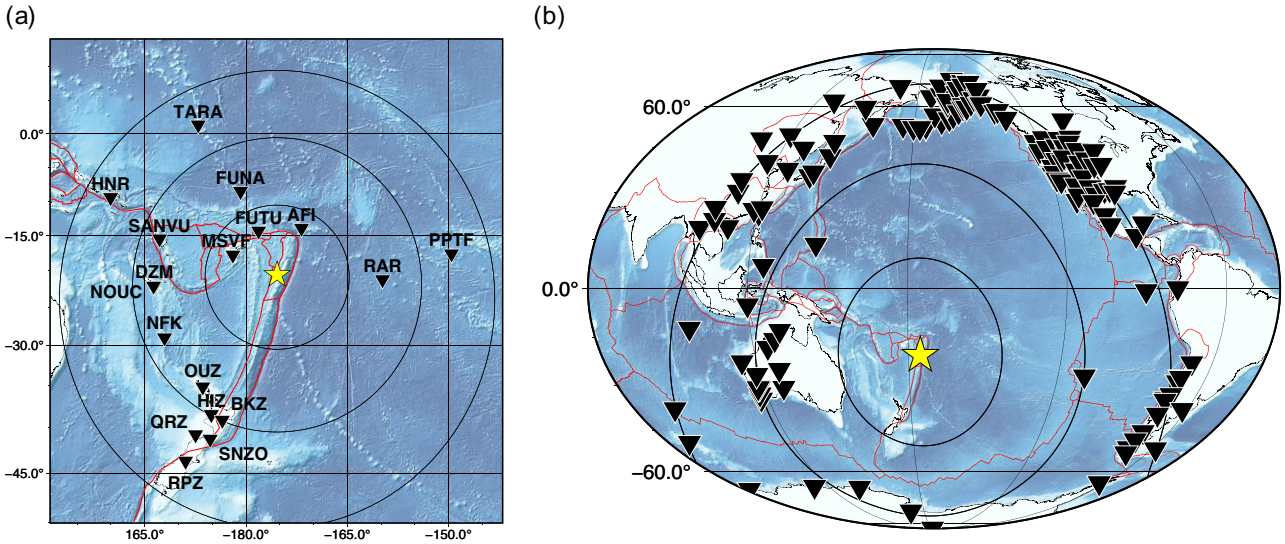

Figure 1. Source-station geometry and tectonic setting. The yellow star is centred on the epicentre of the seismic sequence, at HTTH volcano. Plate boundaries (in red) are from Bird (2003). (a) Regional stations (18) used in the analysis of surface waves. Concentric circles are at distances of 10°, 20°, and 30° from the source. (b) Teleseismic stations (142) used in the analysis of *P* waves. Concentric circles are at distances of 30°, 60°, and 90° from the source.

4 ESTIMATING A SINGLE SUBEVENT

We performed 25 inversions to determine the most likely source model for the first subevent in the HTHH eruption sequence (Table 2). Each inversion involved performing a grid search in the model parameter space of point forces or moment tensors using the open-source Python code MTUQ. MTUQ implements the 'cut-and-paste' algorithm of Zhu & Helmberger (1996) to mitigate the effects of 3-D velocity structures that are unaccounted for with our assumed reference 1-D model, AK135f (Montagner & Kennett 1996). It does so by allowing time-shifts of the generated synthetic seismograms, compensating for the difference between theoretical and observed arrival times.

To generate the synthetic waveforms, we used a Green's functions database computed for AK135f using the spectral element solver AxiSEM (Nissen-Meyer *et al.* 2014), obtained from the IRIS DMC Syngine web service (Krischer *et al.* 2017), and parsed using Instaseis for efficient buffered I/O (van Driel *et al.* 2015). The Green's functions in the database are accurate down to periods of 2 s. We use a 5 s trapezoid source wavelet to convolve the Green's function database before filtering. We measured the goodness of fit of each source parameter by computing the sum of least-squares misfit between observed and synthetic waveforms and exploring the whole parameter space to find the source parameters that provide the best-fitting synthetics.

Two grid search categories are conducted to estimate the seismic source of the first subevent. For moment tensors, the search covers depth, magnitude, source type and orientation; for forces, the search covers depth, amplitude and direction. The discretization

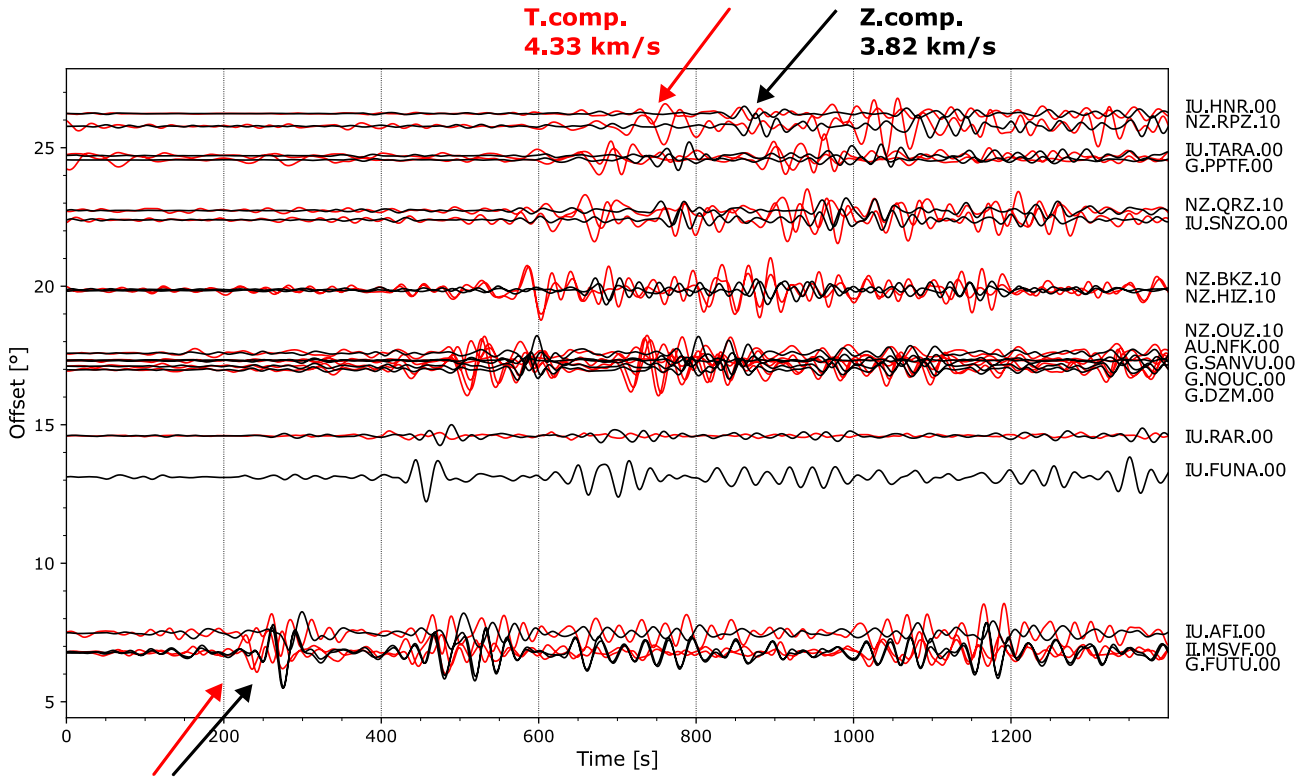

Figure 2. Surface wave record section of 18 regional stations for transverse (red) and vertical (black) components. Both components have been bandpass-filtered between 25–70 s. The amplitude of the transverse component signals have been multiplied by a factor of 1.61 to enhance visibility. The linear moveouts of both surface waves are highlighted by arrows on both ends of the plot, revealing different velocities, which is consistent with the hypothesis that the transverse component signals are Love waves (4.33 km s^{-1}), while the vertical component signals are Rayleigh waves (3.82 km s^{-1}). At the set of 142 more distant stations (71° to 98°) and considering the same bandpass as here, the median amplitude ratio for the transverse component to vertical component is 0.5.

details and explored parameter ranges are provided in Thurin & Tape (2023). The grid searches were conducted on a high-performance computing cluster, taking advantage of MTUQ parallelization, and involved up to 1.9×10^9 evaluations of a waveform misfit function (one evaluation per source).

In the following subsections, we compare the results from the force and moment tensor models using a set of comparable parameter explorations to provide an unbiased comparison of the two source models for the first subevent in the sequence.

4.1 Force results

The results of force parameter estimation using teleseismic and regional data are shown in Fig. 4. The first three rows represent the results of our parameters exploration plotted on the unit sphere, which we will refer to as the *force sphere*. The grey arcs on the sphere surface denote the west and east directions, the south direction splits the plot to the left and right, and the north direction is represented by the boundary of the plot.

The best-fitting force for teleseismic *P* waves is a subvertical downward force with a slight deflection from the vertical axis toward the northwest (Fig. 4a). Figs 4(b) and (c) provide information on the best amplitude and depth with respect to the force direction, respectively, highlighting the non-trivial trade-offs between all of the force parameters. (A *trade-off* exists when a parameter change, such as decreasing depth, is accompanied by a change in a different parameter, such as the force direction or amplitude, in order to achieve the best possible waveform fits.) Finally, the misfit-versus-depth plot in Fig. 4(d) reveals trade-offs between depth and force amplitude. It indicates that the best waveform fit is achieved for 28 km depth, which seems unrealistic given the shallow nature of the volcanic eruption.

The best-fitting force for regional surface waves is also subvertical with a deflection toward the northwest direction (Figs 4e). The deflection from vertical is more pronounced than in the body-wave results. The transverse signal likely brings some additional constraints to retrieve the non-vertical component of the force, as a purely vertical force applied onto the surface would not generate any transverse motion (Runs SF11 and SF12 of Table 2). The low misfit area at the top half of the force sphere in Fig. 4(e) is symptomatic of cycle-skipping, as it shows that flipping the sign of the synthetics would fit the observed data almost as equally well as the minimum solution. Figs 4(f) and (g) share the same characteristic shape, which again denotes the strong trade-offs among force direction, amplitude, and depth. Finally, Fig. 4(g) shows that the best-fitting depth is located at 11 km. Most of the misfit values displayed here are within the range of 1 per cent of variation from the minimum misfit, hinting at nearly equivalent synthetics across all depths.

4.2 Moment tensor results

An earthquake-like point-source can be mathematically represented by a 3×3 symmetric matrix—known as a moment tensor M—which

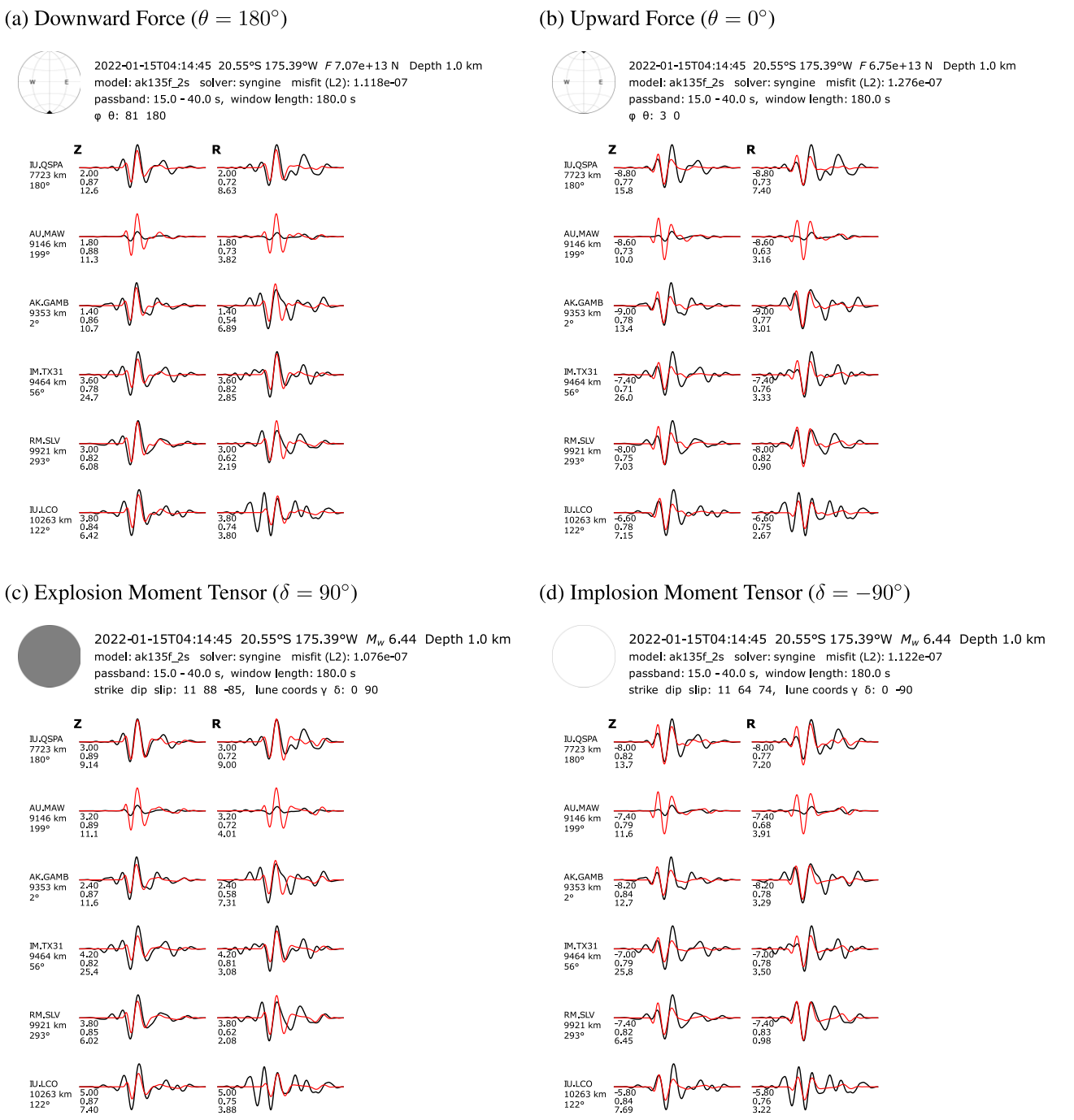

Figure 3. Subset of *P* waveform fits for four trial sources for a fixed depth of 1 km. The only search parameter is magnitude. All four sources provide reasonable waveform fits. The Earth model used for calculating the synthetic seismograms is AK135f (Montagner & Kennett 1996). For such a radially symmetric Earth model, these four end-member sources produce no transverse-component wavefield. (a) Downward force (Run SF10). Stations ID, distance, and azimuth are denoted on the left of each row. Waveform components [vertical (*Z*) and radial (*R*)] are denoted above each column. The three numbers beneath each waveform denote time-shift (seconds), correlation coefficient (0–1), and percent contribution to the total misfit. (b) Upward force (Run SF9). (c) Explosion moment tensor (Run SM10). (d) Implosion moment tensor (Run SM9).

can be represented by its decomposition $M = U[\mathbf{\Lambda}]U^T$. The eigenvalues $\mathbf{\Lambda} = (\lambda_1, \lambda_2, \lambda_3)$ provide the magnitude and source type, via the norm of $\mathbf{\Lambda}$ and the direction of $\mathbf{\Lambda}$ on the eigenvalue lune, which is represented by lune longitude and lune latitude (Tape & Tape 2012). The orientation of M is represented by U, which contains the eigenvectors and can be calculated from strike, dip, and rake angles, which are physically most meaningful for double-couple moment tensors. The moment tensor has been used to represent non-seismic events, such as landslides, explosions, mine collapses, and volcano-tectonic events. Readers may refer to table 1 of Alvizuri & Tape (2016) for a list of references in these settings.

Table 2. Summary of settings for 25 grid search runs for the main subevent. An expanded version of this table can be found in Thurin & Tape (2023). In Runs SF1–SM4, the depth was varied. In Runs SF5–SM8, the depth was fixed to 1 km. In Runs SF9–SM12, both the source and the depth were fixed. For all runs, the force amplitude or moment magnitude was varied.

Run	force	MT	Surf-*Z*	Surf-*R*	Surf-*T*	*P*–*Z*	*P*–*R*	Depth
SF1	X	–	–	–	–	X	X	0–60
SF2	X	–	X	X	X	–	–	0–30
SF3	X	–	X	X	–	–	–	0–30
SF4	X	–	X	–	–	–	–	0–30
SM1	–	X	–	–	–	X	X	0–60
SM1-X	–	X	–	–	–	–	–	0–16
SM2	–	X	X	X	X	–	–	0–30
SM3	–	X	X	X	–	–	–	0–30
SM4	–	X	X	–	–	–	–	0–30
SF5	X	–	–	–	–	X	X	1
SF6	X	–	X	–	–	–	–	1
SF7	X	–	X	X	–	–	–	1
SF8	X	–	X	X	X	–	–	1
SM5	–	X	–	–	–	X	X	1
SM6	–	X	X	–	–	–	–	1
SM7	–	X	X	X	–	–	–	1
SM8	–	X	X	X	X	–	–	1
SF9	X	–	–	–	–	X	X	1
SF10	X	–	–	–	–	X	X	1
SM9	–	X	–	–	–	X	X	1
SM10	–	X	–	–	–	X	X	1
SF11	X	–	X	X	X	–	–	1
SF12	X	–	X	X	X	–	–	1
SM11	–	X	X	X	X	–	–	1
SM12	–	X	X	X	X	–	–	1

Our primary moment tensor results for the main subevent are shown in Fig. 5. The first three plots of each row are analogous to the first three rows of Fig. 4. Results are mapped onto the surface of the eigenvalue lune, which has the double couple at centre (1, 0, −1), the explosion at top (1,1,1) and the implosion at bottom (−1, −1, −1).

The best-fitting moment tensor for teleseismic *P* waves is an explosive-like source, with all the energy radiated outward but not in a spherically symmetric fashion (Fig. 5a). Similarly to the force results, we see in Figs 5(b) and (c) some non-trivial patterns emerging from the misfit space, such as a strong dependency among source type (explosion-like or implosion-like), depth, and magnitude, with all parameters being tightly connected. The misfit-versus-depth plot indicates that the best-fitting moment tensor is located at a depth of 13 km, with a magnitude of M_w 6.42 (Fig. 5d).

The best-fitting moment tensor for regional surface waves is also located in the explosive-like upper region of the lune (Fig. 4e) and exhibits the characteristic low misfit-swath crossing the lune from top to bottom, commonly observed in shallow nuclear test events (Ford *et al.* 2010, 2012; Alvizuri & Tape 2016, 2018). From the magnitude and depth trade-offs maps in Figs 4(f) and (g), we see that the preferred solution is a shallow explosive-like source radiating energy outward in all directions.

For both the force and the moment tensor models, the polarity of the source is consistent, as downward forces and explosive-like sources produce comparable axially symmetric radiation patterns (Fig. 3). From the four misfit-versus-depth plots in Figs 4 and 5, only the moment tensor inversion using surface waves returns a very shallow depth (1 km) for its best-fitting solution (Fig. 4h).

Our grid searches suggest that a downward reaction force to jetting and an explosive-like moment tensor are the most probable source models, and it is reasonable to assume that these phenomena would occur in the near-surface portion of the volcano. Therefore, for the remaining analysis, we use a fixed depth of 1 km, as it is the only very shallow depth to come out of our grid searches. However, both surface wave depth plots (Figs 4h and 5h) suggest that the depth resolution is poor: despite the 30 km depth range considered in our searches, the waveform misfit variations are relatively small.

Results of force and moment tensor grid searches with a fixed depth of 1 km are shown in Fig. 6. In both cases, the two data sets—*P* and surface waves—do not have the same sensitivity to magnitude (with a strong discrepancy between body and surface wave amplitude/magnitude) and source types. Nevertheless, they all produce the same coherent source polarity: positive/downward radiations away from the volcano.

5 ESTIMATING FOUR SUBEVENTS

We now consider the sequence of four subevents (S1–S4). Assuming that all subevents occurred at the same location (−175.390°, −20.546°, 1 km), the previous results for subevent S1 provide constraints that can be used to jointly invert the source parameters and onset times of each subevent. This approach provides a more natural characterization of the sequence and avoids potential biases from sequential determinations of the source parameters. The time-shifts obtained from the best-fitting downward force and explosive moment tensor (available along with waveform fits in Thurin & Tape 2023) enable us to use the path-calibration method proposed by Shi *et al.* (2018). This approach has been previously used to invert multiple subevents over a large earthquake rupture to represent the complex spatial and temporal characteristics of the rupture by a series of point sources.

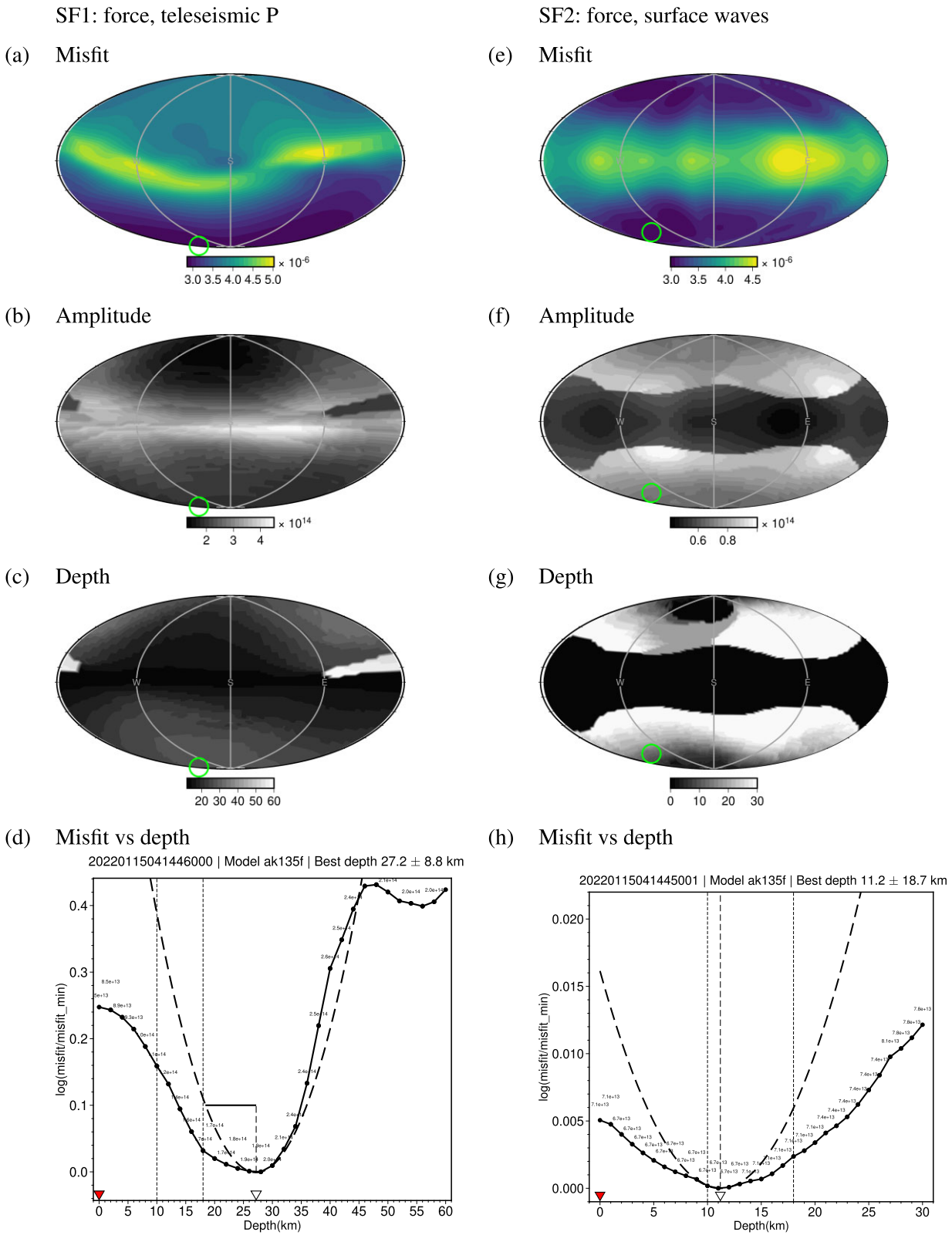

Figure 4. Force results using (a)–(d) teleseismic *P* waves and (e)–(h) regional surface waves. The two cases correspond to Runs SF1 and SF2 in Thurin & Tape (2023), which contains expanded results and corresponding waveform fits. (a) *P* waveform misfit as a function of force direction, with each direction having an amplitude given by the map in (b) and a depth given by the map in (c). The best-fitting force is plotted as a green circle and points downward. (b) Best-fitting force amplitude (1.0 x 10 ^{14} N) for each force direction, considering all depths. (c) Best-fitting depth (km) for each force direction, considering all force amplitudes. (d) *P* waveform misfit as a function of depth. The text label at each depth is the best-fitting force amplitude. The overall best-fitting depth is 27 ± 9 km. (e)–(h) Same as (a)–(d), but for regional surface waves. The overall best-fitting depth is 11 ± 19 km.

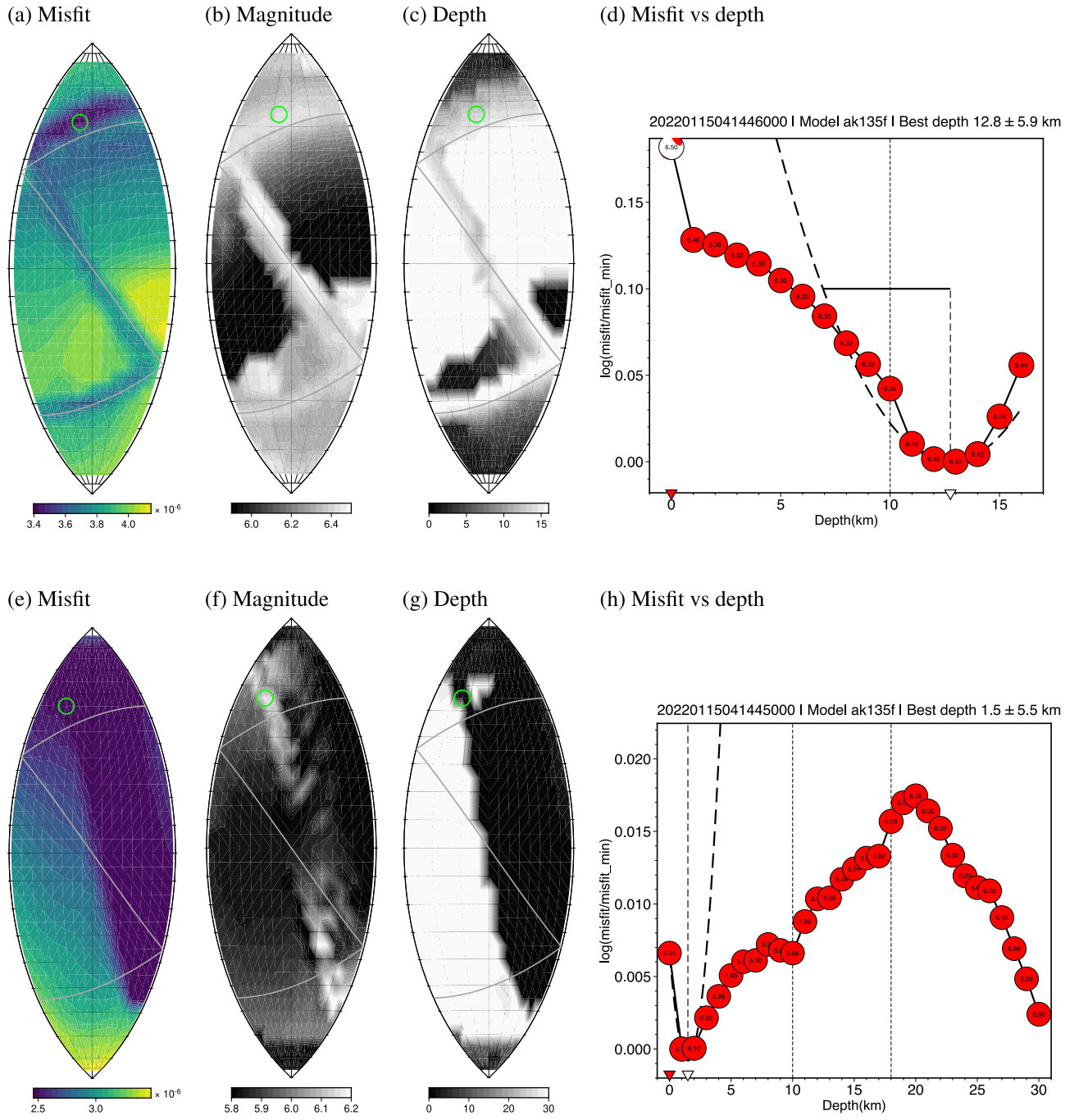

Figure 5. Moment tensor results using (a)–(d) teleseismic *P* waves and (e)–(h) regional surface waves. The two cases correspond to Runs SM1-X and SM2 in Thurin & Tape (2023), which contains expanded results and corresponding waveform fits. (a) *P* waveform misfit as a function of moment tensor source type, with each direction (lune longitude and lune latitude) having a magnitude given by the map in (b) and a depth given by the map in (c). (b) Best-fitting magnitude (M_w) for each moment tensor source type, considering all depths and moment tensor orientations. (c) Best-fitting depth (km) for each moment tensor source type, considering all magnitudes and moment tensor orientations. (d) *P* waveform misfit as a function of depth. The beachball depicts the best-fitting moment tensor at each depth; the text label is the corresponding magnitude. The overall best-fitting depth is 13 ± 6 km. (e)–(h) Same as (a)–(d) but for regional surface waves. The overall best-fitting depth is 1 ± 5 km.

5.1 Subevent onset times

As shown in Fig. 3, cycle-skipping can introduce ambiguity and complicate the joint inversion of source parameters. In order to reduce cycle-skipping, we turn to high-frequency vertical teleseismic *P*-wave recordings to define appropriate onset time bounds for each subevent. We examined vertical displacement seismograms from 86 teleseismic stations from an epicentral range of 70°–98°, high-pass filtered above 0.005 Hz (causal filter). We aligned the waveforms, stacked them, and measured the relative timing among subevents (Fig. 8). Due to the high noise levels in the stacks, it is difficult to confidently determine the absolute timing of the first motions in the sequence, which is why we rely on the relative timing of the maxima on the vertical and radial displacements.

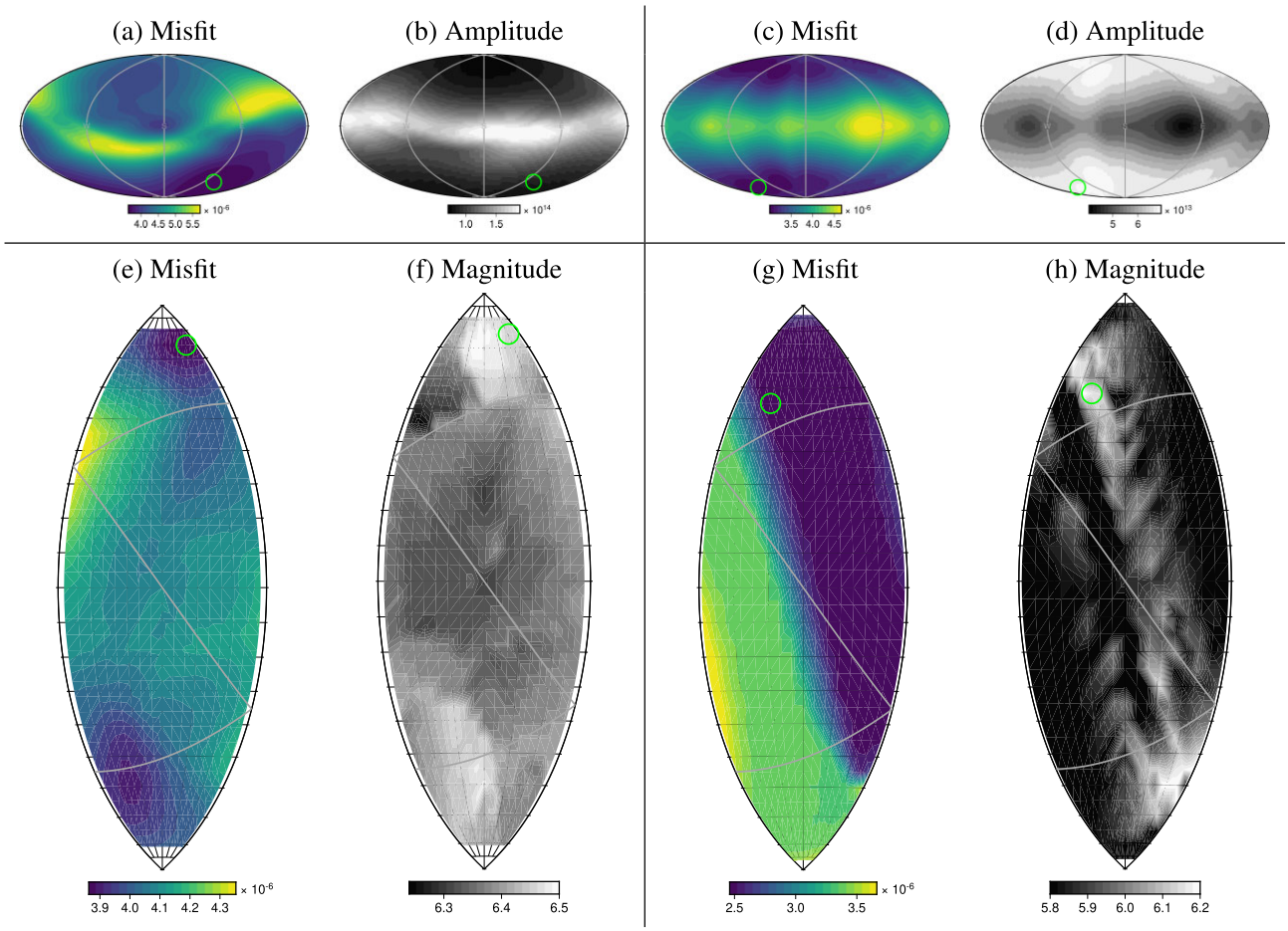

Figure 6. Waveform misfit plots for (a)–(d) force and (e)–(h) moment tensor assuming a fixed depth of 1 km. The four cases correspond to Runs SF5, SF8, SM5 and SM8 in Thurin & Tape (2023), which contains expanded results and corresponding waveform fits. The best-fitting source (depicted as a green circle) is either adownward force (a and c) or an explosion-like moment tensor (e and g). (a) *P* waveform misfit as a function of force direction, with each direction having an amplitude given by the map in (b). (b) Best-fitting force magnitude for each force direction. (c) and (d) Same as (a) and (b), but for surface waveforms (*Z*+*R*+*T*). (e) Surface waveform misfit as a function of moment tensor source type, with each direction (lune longitude and lune latitude) having a magnitude given by the map in (f). (f) Best-fitting moment magnitude for each moment tensor source type. (g) and (h) Same as (e) and (f), but for surface waveforms (*Z*+*R*+*T*).

We chose a ±10 s allowable time range for each onset-time search (Fig. 8, vertical yellow bands) in order to limit the search within half a period of the filtered data set (which should help prevent cycle-skipping) and make sure there are no possible overlaps between subevents. In the following regional surface waves inversion, we will simultaneously invert for the source parameters and the relative onset times of four subevents within the defined ±10 s time windows centred on the relative *P*-wave peaks measured in Fig. 8.

5.2 Model parameter space

The model parameters we have searched over are listed in Table 3, along with their allowable ranges within the inversion. For each subevent i, we will consider two potential candidate sources: a point force source with four parameters (t_i, $\|\mathbf{f}_i\|$, ϕ_i, h_i) representing onset time in seconds, force amplitude in Newtons, and force direction in terms of azimuthal angle ϕ and polar angle θ ($h = \cos\theta$); and a moment tensor source with seven parameters (t_i, m_i, δ_i, γ_i, κ_i, σ_i, h'_i) representing onset time in seconds, moment magnitude in M_w, lune latitude and longitude, and strike, rake, and dip angles ($h' = \cos\theta'$). In total, we have 16 free parameters for the four-subevent force inversion and 28 for the moment tensor inversion.

5.3 Experimental setup

We seek to find the optimal set of four forces F_i and moment tensors M_i along with their onset times t_i, with $i = [1, 2, 3, 4]$, that minimizes

$$f(F_i, t_i) = \|d_{\text{syn}}(F_i, t_i) - d_{\text{obs}}\|_2 \quad (1)$$

and

$$f(M_i, t_i) = \|d_{\text{syn}}(M_i, t_i) - d_{\text{obs}}\|_2 \quad (2)$$

where $F_i = (\|\mathbf{f}_i\|, \phi_i, \theta_i)$ parametrizes the point force and $M_i = (m_i, \delta_i, \gamma_i, \kappa_i, \sigma_i, h'_i)$ parametrizes the moment tensor (Table 3), d_{obs} is the set of observed waveform data in the vertical, radial and transverse components for the set of stations, and $d_{\text{syn}}(F_i, t_i)$ and $d_{\text{syn}}(M_i, t_i)$ are the set of synthetic waveforms computed for each source by summation of four time-shifted synthetics (one for each

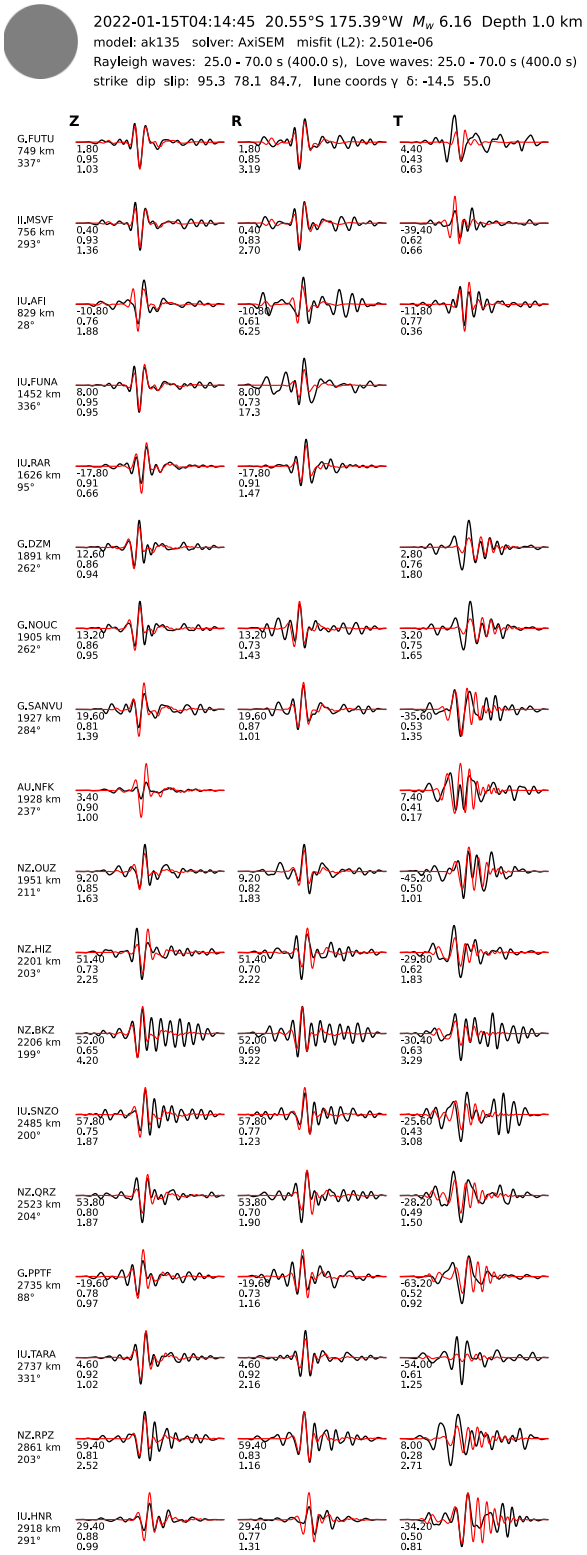

Figure 7. Surface wave fits for the best-fitting moment tensor and depth (Run SM2). The best-fitting depth of 1 km was used for the fixed-depth runs (Table 2), as well as for the multi-subevent runs (Section 5). Numbered annotation for each row and waveforms are the same as in Fig. 3. The third column denotes the transverse (*T*) components. Time-shifts already include a 51 s static time-shift to account for inaccurate origin time.

subevent), following

$$d_{\mathrm{cal}} = \sum_{i=1}^{4} (\tau_i * \mathcal{G} M_i) \tag{3}$$

where τ_i is a discrete Gaussian function centred on onset-time t_i that is used to shift the signal in time, $*$ denotes the convolution operator and $\mathcal{G}$ is the set of Green's function for each source–receiver pair in the considered data set. Likewise, the synthetics associated with the force model are constructed using the appropriate set of Green's functions. As in the case with the single-subevent inversions, the synthetics are computed in the AK135f velocity model using a 1 km deep source.

We have chosen to define τ_i as a discrete Gaussian random variable with $\mathcal{N} \sim (t_i, (0.17)^2)$, which results in discrete Gaussian peaks with a characteristic duration of the order of 1 s centered on t_i. Assuming the sources are impulsive, the purpose of the Gaussian function is to shift the function in time, and we consider the source-time function as a sum of Gaussian peaks with a finite duration. To our knowledge, only Garza-Girón *et al.* (2023) have employed a similar impulsive-like source representation for inverting the source-time function of the HTHH. In their study, they defined the source-time function as a sum of 4-s Gaussian impulses.

To efficiently search the model parameter space and find the minimum of eqs (1) and (2), we use the covariance matrix adaptation evolution strategy (CMA-ES, Hansen & Ostermeier 2001), which is described in Appendix A. In the following, we define our parametrization for a single subevent, which can be generalized to the complete sequence of four considered subevents. We work with two distinct spaces to simplify parameter handling and scaling (Fig. 9). The first is the non-uniform, bounded, 'physical' parameter space (Φ-space) that directly relates to each of the source parameters k (4 for the force sources and 7 for the moment tensor source) for each subevent (Table 3). The second is a uniform, bounded, CMA-ES-space (Ξ-space) that contains k variables per subevent; all bounded in [0,10].

In practice, the CMA-ES does not require any parameter tuning and can be initialized to the default values for μ, w, c_σ, d_σ, c_c, c_1 and c_μ as determined by Hansen & Ostermeier (2001, we will, however, use a different number of offspring λ). Readers may refer to Hansen *et al.* (2015) and Hansen (2016) for a complete overview of the CMA-ES algorithm and existing implementations.

During each iteration of the algorithm, the CMA-ES draws samples from the Ξ-space and projects each offspring onto the Φ-space to compute the misfit value. The parameters t_i and m_i have arbitrarily determined bounds, while the other parameters have bounded domains determined by geometrical considerations. After the misfit values of each sample are computed in Φ, updates and adaptation occur in the uniform CMA-ES space Ξ.

In the following section, we detail results from the HTHH regional surface wave data analysis utilizing CMA-ES and $\lambda = 2400$ samples. This larger sample size, two orders of magnitude greater than the default (Hansen 2016), delivered consistent outcomes across multiple realizations with uniform randomized initialization and generated smoother optimization paths in Φ. Lastly, we employed static time-shift corrections to the 1 km depth grid search synthetic data for path calibration.

Since we applied static time-shift corrections to our traces prior to the inversion, our application is reminiscent of the Markov-Chain Monte-Carlo application of Shi *et al.* (2018), but using a different optimization algorithm that is directly interfaced with the MTUQ classes and methods. Our CMA-ES implementation uses mpi4py

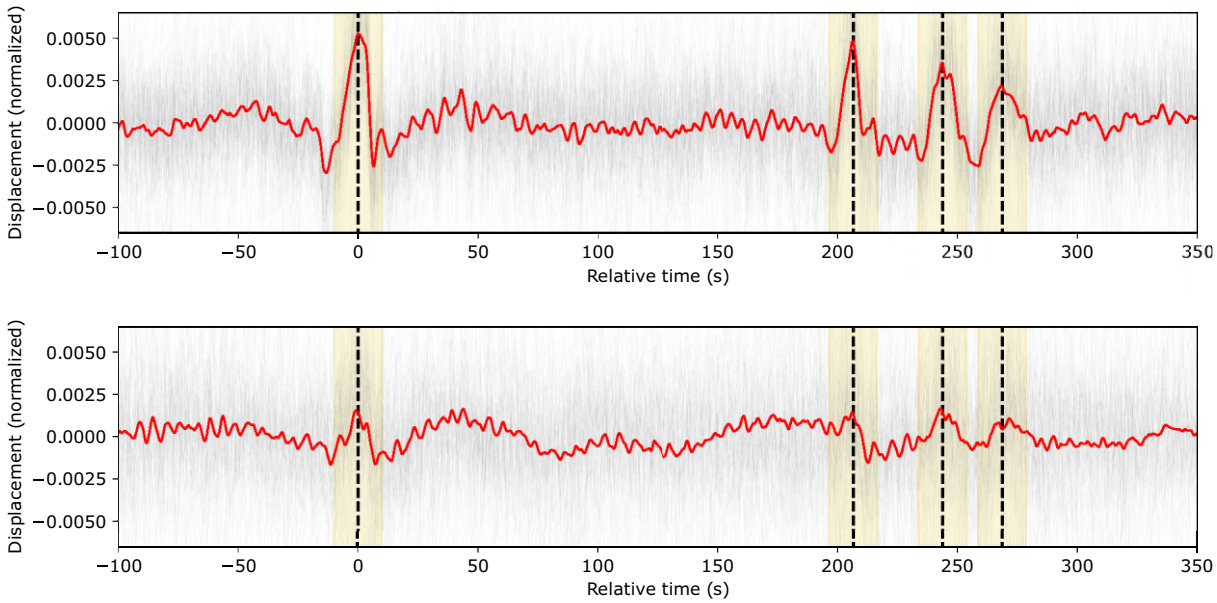

Figure 8. Vertical component (top) and radial component (bottom) stacks (in red) of the teleseismic *P*-wave signals, high-pass filtered above 0.005 Hz (causal filter). The stacked waveforms are plotted in grey beneath the stack. Measured peaks are denoted by dashed vertical black bars. The onset time windows of ±10 s considered in our tests are denoted by yellow-shaded areas. The differential onset times with respect to the first peak are: 205.60 s (S2–S1), 243.78 s (S3–S1) and 268.57 s (S4–S1); and other differential times are 37.18 s (S3–S2), 61.97 s (S4–S2) and 24.78 s (S4–S3).

Table 3. Model parameters in this study, along with their allowable ranges. There are 4 sets of 7 inversion parameters, for a total of 28 parameters. The onset time t_0 for each subevent is determined from the stack of *P* waveforms (Fig. 8).

Parameter	Variable	Min	Max
Force, polar angle	θ	0°	180°
	$h = \cos(\theta)$	−1	1
Force, azimuthal angle	ϕ	0°	360°
Force, amplitude	$f = \|\mathbf{f}\|$	10^{12} N	10^{16} N
Moment magnitude	$m = M_w$	5.5	6.5
Eigenvalue lune longitude (source type)	γ	−30°	30°
Eigenvalue lune latitude (source type)	δ	−90°	90°
Strike angle (orientation)	κ	0°	360°
Dip angle (orientation)	θ'	0°	90°
	$h' = \cos(\theta')$	0	1
Rake angle (orientation)	σ	−90°	90°
Subevent onset time	t	$t_0 - 10$ s	$t_0 + 10$ s
Longitude (hypocentre)	x_s	−175.390° (fixed)	
Latitude (hypocentre)	y_s	−20.546° (fixed)	
Depth (hypocentre)	z_s	1 km (fixed)	

(Dalcin & Fang 2021) to leverage the embarrassingly parallel nature of the algorithm and execute the filtering, synthetics generation, and misfit measurements by distributing independent pools of samples over CPU cores.

5.4 Force results

We first applied the CMA-ES to explore the space of parameters for a point force source. We performed 10 separate searches with up to 400 iterations (9.6×10^5 misfit evaluations). (We refer to these 10 searches as *realizations*.) The initial mean for each of the 16 parameters was drawn from a uniform distribution spanning [0,10] such that each realization would have a random starting position. The onset time bounds for this set of inversion were restricted at ±10 s of the picked displacement maximum in Fig. 8.

Inversion results for subevents S1 (blue), S2 (orange), S3 (red) and S4 (green) along with the projected 'optimization' path on the force sphere for the 400 iterations are represented in Fig. 10. Consistent solutions are achieved in most of the realizations, with several solutions reaching the same misfit. Each realization converges toward various combinations of upward and downward forces that fit the observations, even though there is a tendency toward a series of downward forces tilted toward the northwest direction, as in the previous grid search results for the main subevent. The three best-fitting solutions are all downward forces.

Convergence details for the 10 realizations are displayed in Fig. 11. From Fig. 11(a), we see that after starting from a set of random source parameters yielding a high misfit, the CMA-ES quickly converges toward low misfit values. Figs 11(b) and (c) shows the four subevents' amplitude and total amplitude, plotted versus the

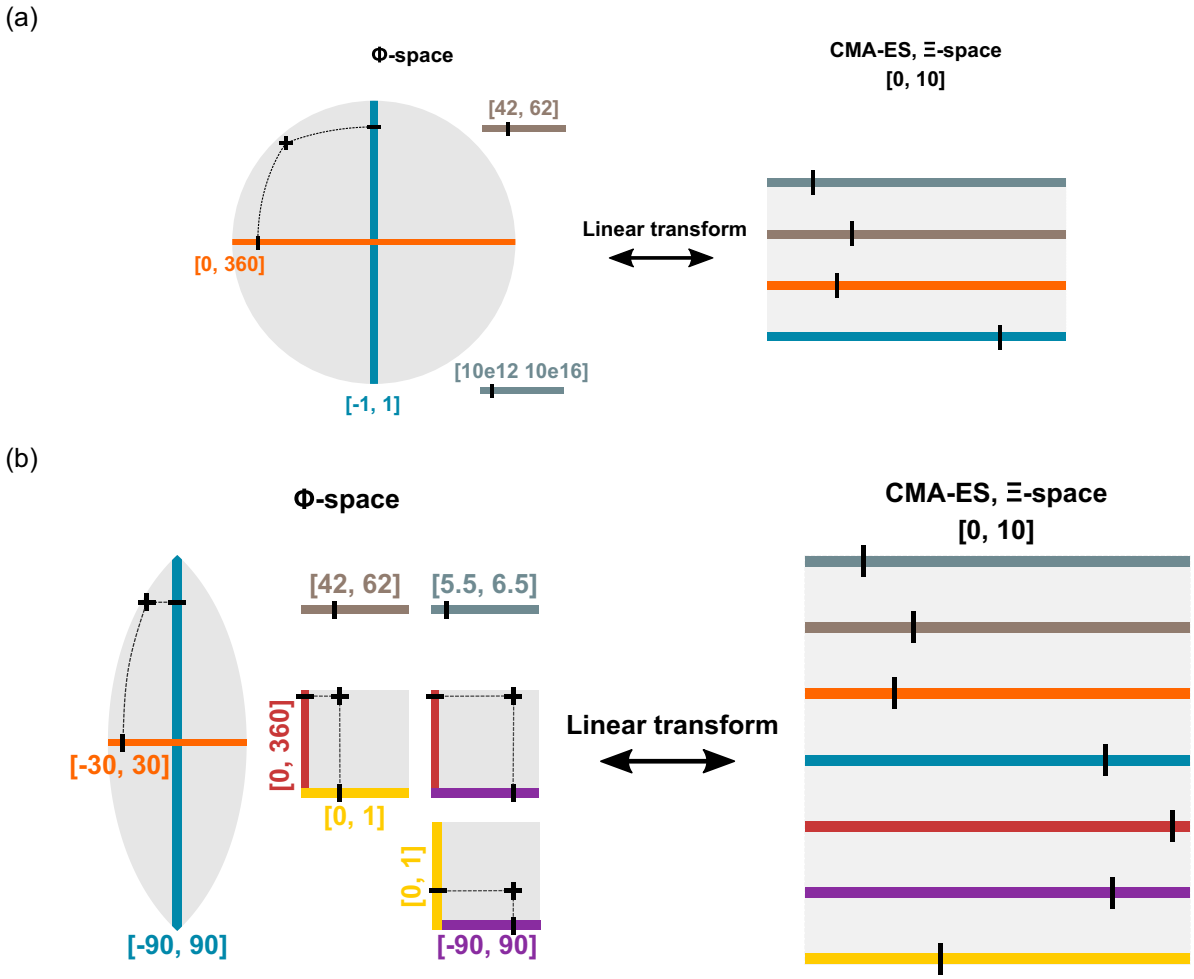

Figure 9. Schematic representation of model parameter spaces for (a) force and (b) moment tensors. The physical space is Φ and the CMA-ES space is Ξ; see also Table 3. Samples are drawn in a uniform random manner from Ξ space and projected onto the various physical domains in Φ. (a) The colour code is slate-grey for $\|\mathbf{f}\|$ (force amplitude), brown for t_0 (range of ±10 s), orange for ϕ (azimuthal angle in degree), blue for $h = \cos\theta$ (dimensionless), where θ is the polar angle. (b) The colour code is slate-grey for m (moment magnitude), brown for t_0, orange for δ, blue for γ, red for κ, purple for σ (angles in degrees) and yellow for $h' = \cos(\theta')$ (dimensionless), where θ' is the dip angle.

number of iterations. Although we observe some slight variations in the estimated amplitude, the general trend is that the amplitude gets smaller after each subevent. The cumulative amplitude shown in Fig. 11(c) is estimated at $(1.7 \pm 0.1) \times 10^{14}$ N. Fig. 11(d) reveals the occurrence of subevents for some realizations having upward-pointing forces ($\theta \approx 0°$), representing cycle-skipping. This can be inferred because the upward forces are associated with onset times that are at the edge of the allowable time-search windows.

5.5 Moment tensor results

We performed an analogous set of 10 realizations using a moment tensor source instead of a force source, resulting in a change from 16 to 28 source parameters for the four subevents. The outcomes of the inversions for subevents S1 (blue), S2 (orange), S3 (red), and S4 (green) are consistent for all 10 realizations (Fig. 12): all subevents are explosive source types represented by moment tensors having all-positive eigenvalues. Note that despite each outcome being a series of four explosions, there are still variations within the isotropic-eigenvalue region of the lune. Subevent S1 exhibits peculiar behaviour, having only two possible solutions. In most cases, all four moment tensor solutions first converge toward the centre of the lune (where the double-couple solution resides), as the initial multivariate Gaussian distribution tends to grow during the first few iterations, then all four beachballs converge toward the upper portion of the lune.

Misfit curves for all 10 realizations are shown in Fig. 13(a). From one realization to the next, waveform fits are qualitatively indistinguishable, despite the variations of configurations in the explosion sequence. The log-scaled misfit values also illustrate the non-uniqueness of the solution, as all misfit curves converge to the same range of values, despite having different source configurations. We achieve convergence in less than 500 000 total misfit evaluations, which is much less than the number of misfit evaluations in the grid searches for the main subevent.

Fig. 13(b) presents the variation of magnitude for all 10 realizations. There are only a few magnitude configurations that explain the data and have almost equivalent misfits. We also observe a trade-off between magnitude and lune coordinates: for instance, S3 (red) is either located on the top left or top right of the lune. The average cumulative magnitude for the whole sequence, across ten realizations, is M_w 6.5 ± 0.03.

Surface waveform fits for the initial random state, and the converging (best-fitting) source parameters are shown in Fig. 14, with

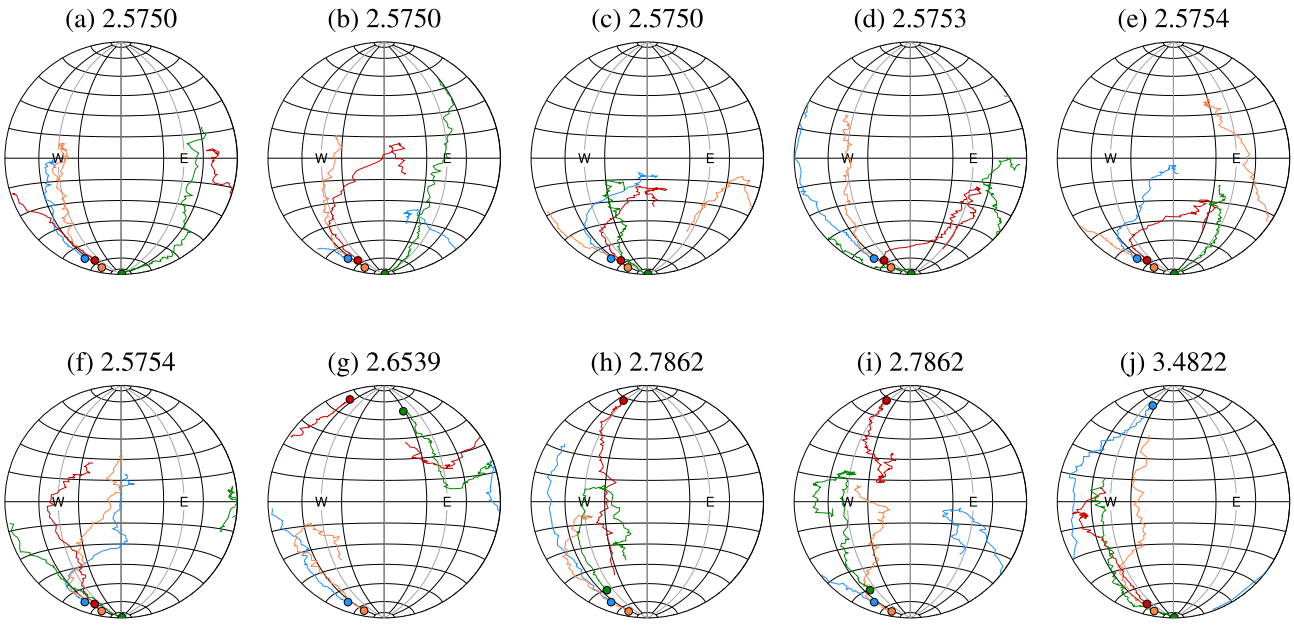

Figure 10. Best-fitting forces for the four-subevent realizations using regional surface waves. Each plot shows the trajectories of subevents S1 (blue), S2 (orange), S3 (red) and S4 (green), plotted on the force sphere. The initial parameters are initialized at random and the final convergence points are denoted by solid coloured circles. The misfit function value for the convergent solution is displayed above each plot, in units of 10^{-5} m; the plots are ordered from (a) lowest misfit to (j) highest misfit. For the lowest-misfit outcomes in (a)–(f), all subevents have force sources pointing downward toward the northwest. For the highest-misfit outcomes in (g)–(j), at least one subevent does not have a downward force. A link to a playlist of movies of the 10 realizations is listed in the Data Availability. Corresponding details, including convergence curves, can be seen in Fig. 11.

the full set of stations shown in Fig. S3 (Supporting Information). Qualitatively, the waveform fits for the initial randomly chosen parameters are poor, as expected, while the fits for the convergent solution are good, including on the transverse component.

Compared with the force inversions, the total waveform misfit from moment tensors is lower than its point-force equivalent, and it is also less variable. It is likely that the moment tensor orientation parameters (κ_i, σ_i, h_i') can accommodate changes in moment magnitude and source type, demonstrating the non-uniqueness of the inverse problem.

6 DISCUSSION

We have estimated force and moment tensor source models for the most energetic seismic sequence (∼270 s) that occurred during the HTHH eruption. Our large-scale grid searches for subevent S1 indicated a greater likelihood of downward force or explosive moment tensor, rather than an upward force or implosion moment tensor. We then performed a joint inversion of the four-subevent sequence using both point-force and moment tensor models.

6.1 Subevent source duration

We assume a short, impulsive source time function for each subevent (approximately 1 s duration), as shown in the example in Fig. 14. Our waveform differences between observation and synthetics are performed for chosen bandpass filters of 15–40 s for *P* waves and 25–70 s for surface waves is motivated by signal-to-noise ratio considerations. These filters eliminate the high-frequency portion of the wavefield that is generated by our assumed short-duration sources but which may not be present in the observed wavefield. The lack of high-frequency radiation in the observed teleseismic *P* waves (Fig. 8) suggests that a longer source duration is possible, perhaps even up to 10 s.

Given the satisfactory waveform fits for the four-subevent inversion based on surface waves, we did not wish to add another degree of freedom to the problem, particularly as the period range considered (25–70 s) limits the resolution we can expect to recover in the time domain. Therefore we opted to retain the simplest possible source representation of four short-span impulses, each with a different onset time, despite potential implications in the recovery of magnitude. Nevertheless, consideration of the high-frequency radiation (or lack thereof) could be helpful in discriminating between force and moment tensor sources.

6.2 Source type and source-time function

Our results demonstrate the possibility of two models for the origin of the seismic signal of the HTHH eruption: a downward force sequence or an explosive moment-tensor sequence, both acting in the superficial region of the volcanic edifice. These models are simple and can explain the regional and teleseismic data, and they do not require complex source-time functions. Deconvolution approaches are sensitive to noise and generally produce source-time functions having more complexity. Assuming a downward force, Garza-Girón *et al.* (2023) combined deconvolution and simulated annealing to obtain a source-time function exhibiting rapidly fluctuating amplitudes. Our source-time function, by design, contains a set of four narrow peaks over the ∼270 s time window of our focus (Fig. 14b). However, we can note some general similarities, such as the partition between S1 and the S2–S4 wave packets, and the differences in results could be attributed to different methodologies between the two studies.

A downward force has been invoked by several authors for the best source model for the HTHH seismic signal (Table 1). The

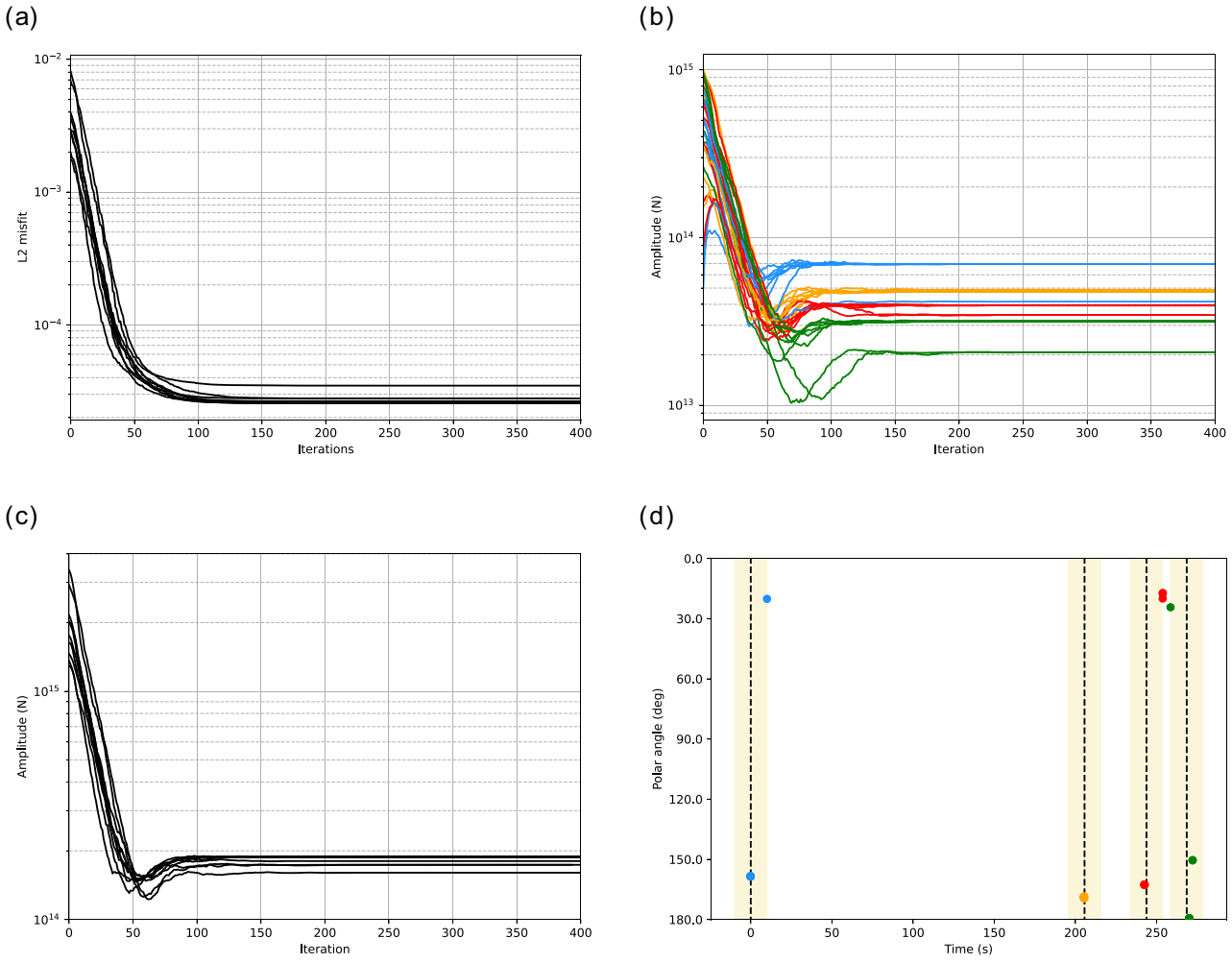

Figure 11. Convergence analysis of the 10 realizations displayed in Fig. 10 for the four-subevent force source. (a) Least-squares misfit. The final average misfit value is $(2.7315 \pm 0.27) \times 10^{-5}$ m. (b) Force amplitude (N) of each subevent: S1 (blue), S2 (orange), S3 (red) and S4 (green). (c) Cumulative amplitude (N), defined as the sum of four amplitudes $\|\mathbf{f}_i\|$. (d) Polar angle θ versus relative onset time in seconds. An upward force is $\theta = 0°$, a downward force is $\theta = 180°$.

downward reaction-force model is compatible with a sustained energy release that varies temporally in conjunction with jetting. However, the explosive-like moment tensor sources suggest a different physical process. The underwater nature of the eruption supports the possibility of Surtseyan activity, involving violent interaction between hot material and water resulting in rapid vapourization of water and production of a large volume of steam, of which a large amount was injected into the stratosphere, as reported by Vömel *et al.* (2022). Distinguishing between the two models based solely on seismic waveforms may not be feasible, and other geophysical models may be necessary to refine the plausibility of each source type.

The potential cause for ambiguity in discerning the source type can be investigated by analysing the eigenvectors and all-positive eigenvalues for the best-fitting moment tensors of subevents S1–S4, shown in Fig. 15. This 3-D representation of the moment tensor provides a perspective on the source geometry that goes beyond the non-informative uniform shading of the isotropic beachball pattern. With this representation, we see that the radiation patterns for S1–S4, represented as ellipsoids, are elongated in the vertical direction and plunging to the northwest. These vertically oriented dipole-like moment tensors share similarities with the optimal point forces that we estimated. See Day & McLaughlin (1991) for a theoretical comparison of force and moment tensor models.

To gain a better understanding of the physical processes underlying the HTHH eruption, future investigations should incorporate supplementary data sources. For instance, hydroacoustic data recorded in the nearby region by MERMAIDS floats (Simons *et al.* 2021) could help refine the origin time using T-phase information. Additionally, the source deduced in our study could be evaluated against plume and tsunami modelling to ascertain whether it meets criteria beyond seismic data alone. Bathymetric and deposit analysis (ejecta size) and plume composition may also serve as valuable indicators of the eruption, potentially helping to resolve the source-type ambiguity.

6.3 Cycle-skipping

This study underscores the pivotal role of precise origin time determination in accurate seismic modelling. Lacking a reliable origin

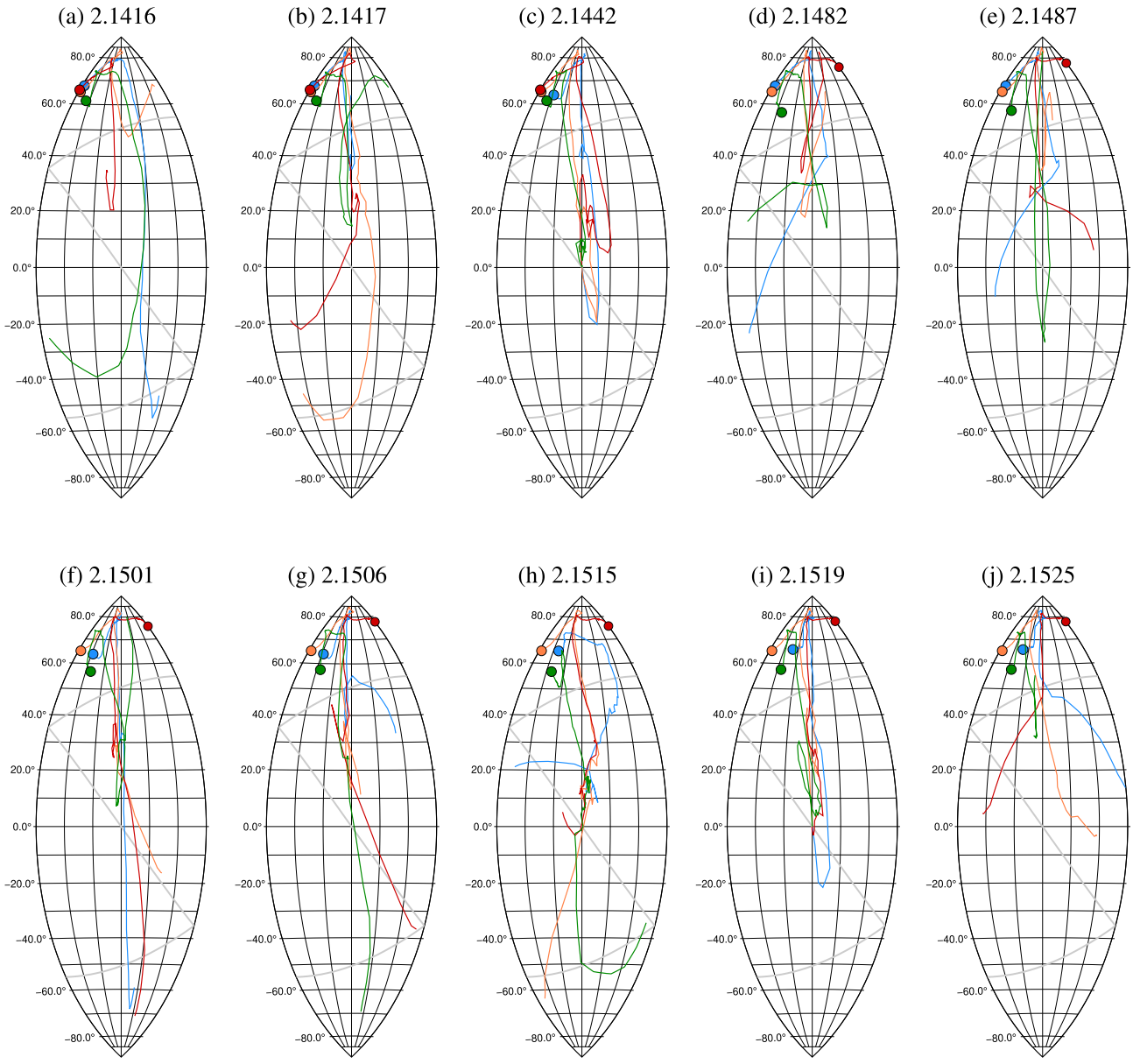

Figure 12. Best-fitting moment tensors for the four-subevent realizations using regional surface waves. Each plot shows the trajectories of subevents S1 (blue), S2 (orange), S3 (red) and S4 (green), plotted on the eigenvalue lune. The initial parameters are initialized at random and the final convergence points are denoted by the corresponding focal mechanism (solid colour for explosions). The misfit function value for the convergent solution is displayed above each plot, in units of 10^{-6} m; the plots are ordered from (a) lowest misfit to (j) highest misfit.A link to a playlist of movies of the 10 realizations is listed in the Data Availability.

time while relying on a 1-D velocity model can lead to the vexing problem of cycle-skipping, whereby the synthetic waveforms are misaligned with observed waveforms because the misalignment offers a quantitatively better cross-correlation value than the true alignment. In Fig. 3, we showed the effect of cycle-skipping on waveform fits for four end-member source models. In Fig. 16, we show how cycle-skipping can impact a large-scale parameter search.

The surface wave-based moment tensor grid search for the main subevent provides intriguing results (Fig. 16). From a depth of 1 km to about 15 km, the best-fitting source type is explosive, and then it transitions to a (lower-magnitude) vertical compensated linear vector dipole-like tensor . The position of the piercing points on the moment tensor (Figs 16c and d) reveals that the polarity of the modelled signal is reversed between the two mechanisms, as most stations fall into the white portion of the beachball. By narrowing the allowable time-shift ranges, in combination with a precise origin time measurement, we could, in theory, improve the source characterization. However, in this study, we have opted to permit cycle-skipping to occur, allowing a wide range of time-shifts in order to avoid bias stemming from the origin time uncertainty and to allow for a more comprehensive exploration of parameter space, relying instead on multiple independent inversions. This enables a better determination of the two more likely source models: downward force and explosive-like moment tensor.

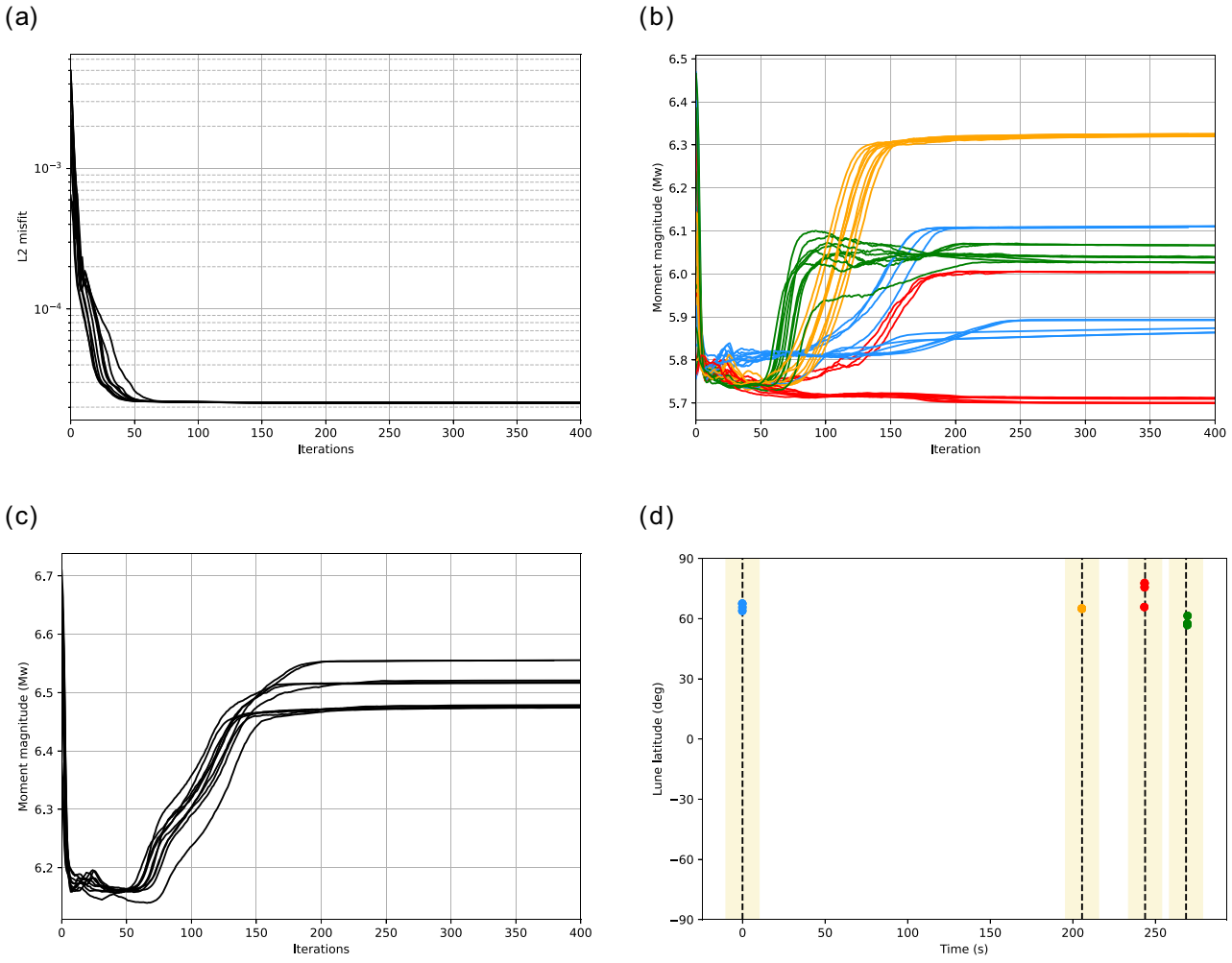

Figure 13. Convergence analysis of the 10 realizations displayed in Fig. 12 for the four-subevent moment tensor source. (a) Least-squares misfit. The final average misfit value is $(2.1481 \pm 0.003) \times 10^{-5}$ m. (c) Magnitude (M_w) of each subevent: S1 (blue), S2 (orange), S3 (red) and S4 (green). (d) Cumulative magnitude (M_w). (b) Lune latitude δ plotted against relative onset time in seconds. A explosion moment tensor is $\delta = 90°$, an implosion moment tensor is $\delta = -90°$.

We previously found that the amount of static time-shift correction required to minimize the lags between observed and synthetic *P* waves was about 32 s (Thurin *et al.* 2022). Since the teleseismic *P*-wave arrival times are expected to be better constrained than the regional surface waves in AK135f, we used *P* waves as the most reliable baseline to constrain the origin time of the main subevent (S1). We also found that an additional correction of 19 s (total of 51 s of static correction) was required to minimize the regional data-to-synthetics time lags, accounting for AK135f being improperly too fast for surface wave propagation in this region. This is reflected in the S1 relative onset time retrieved in Tables 4 and 5, which is given with respect to the USGS origin time.

To refine the origin time estimate, we turn to the results of the fixed depth, 1 km grid search *P* waves results. By averaging the time-shift values over our set of 142 stations for both the best-fitting force and moment tensor at 1 km, we estimate an origin time of 2022-01-15 04:15:19.6 ±1.7 s that accounts for the ambiguity between the two best source models for S1. These results improve on our previous estimate (Thurin *et al.* 2022), which was based on a subset of data.

6.4 Transverse component signals

The global transverse-component signals—visible for all four subevents and interpreted as Love waves (Fig. 2)—may be important for interpreting the physical origin of the seismic signals. Our analysis assumes a simplified Earth model: spherically symmetric AK135f, without bathymetry or topography. In such a model, the end-member sources—explosion, implosion, downward force, and upward force—do not generate *S* or Loves waves (Fig. 3). Therefore, given the presence of observed Love waves, our parameter estimation obtains sources that deviate from these idealized sources. Neglecting the transverse component can significantly impact the estimated source; as shown in Fig. 17, removing the transverse component enables a horizontal—not vertical—force to fit the regional surface wave data.

Importantly, the radiation pattern for Love waves is different for point forces and moment tensors: a point force will generate a two-lobed radiation pattern (Kanamori *et al.* 1984), while the moment tensor source would generally generate a four-lobed radiation pat-

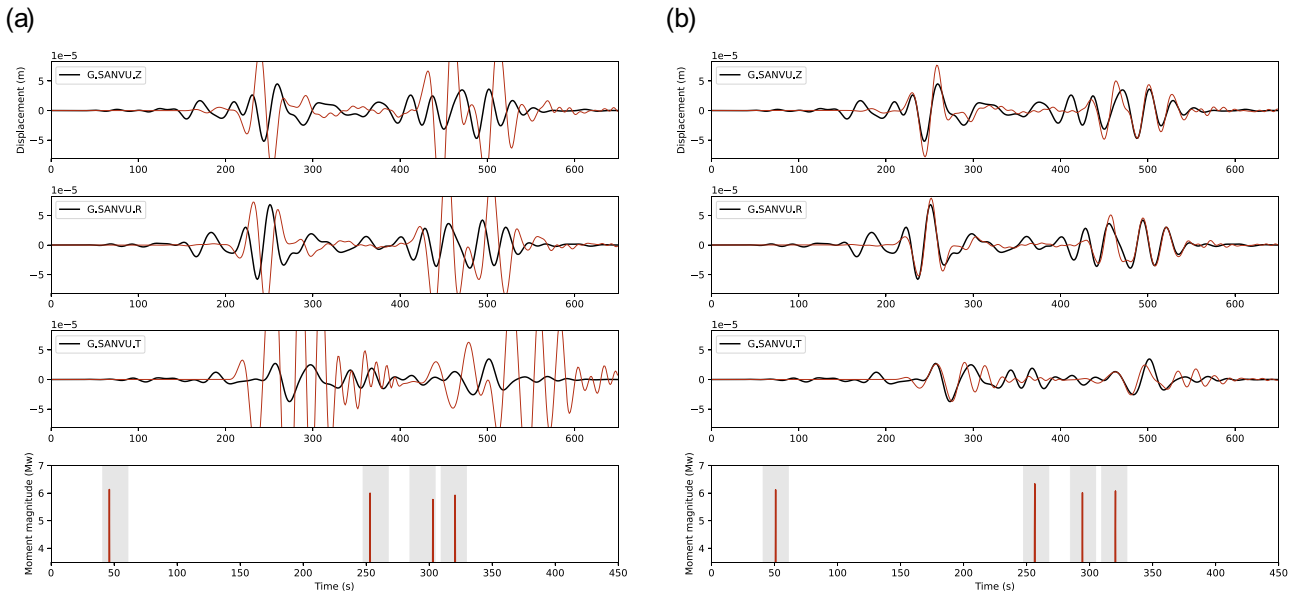

Figure 14. Examples of three-component surface waveform fit for one station for one of the 10 multi-subevent realizations. Seismograms are filtered 25–70 s, with observations in black and synthetics in red. The source model used here is a moment tensor, which differs for each subevent, and the depth is fixed to 1 km. The full display of all waveforms used is shown in Fig. S3 (Supporting Information). (a) Waveform fits for the initial random source parameters for the CMA-ES realization. The fits are expectedly poor. The top three plots are the vertical (top), radial (middle) and transverse (bottom) components. The waveform time-windows include the data considered for the inversion and are, therefore, relative timing (650 s time-window) centred on the surface waves signals. The bottom plot is the source time function with respect to the USGS origin time, with the shaded regions denoting the ±10 s allowable ranges for the four onset times identified in Fig. 8. (b) Waveform fits for the final iteration of the best-fitting realization (Fig. 12a).

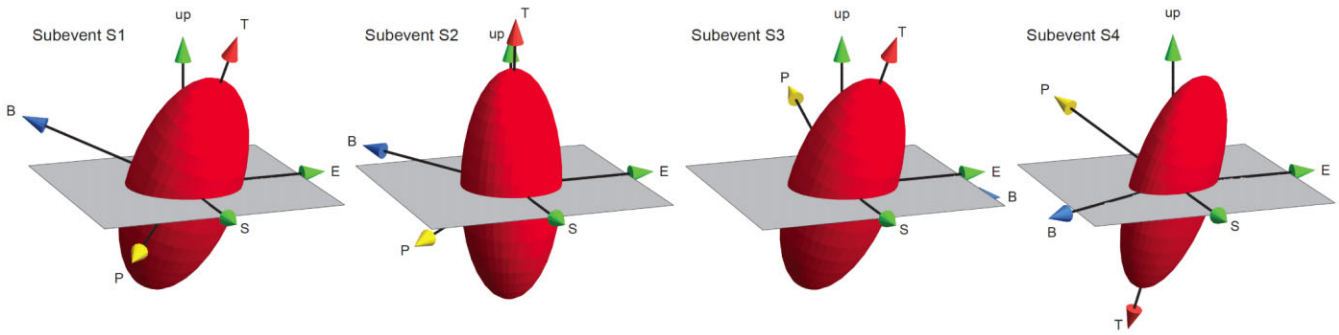

Figure 15. Explosive-like source representation for subevents S1, S2, S3 and S4. The ellipsoids are defined by the eigenvectors (T-B-P) and eigenvalues ($\lambda_1 \geq \lambda_2 \geq \lambda_3 > 0$) of the best-fitting moment tensor. For moment tensors having all-positive eigenvalues, the ellipsoids depict the seismic radiation pattern better than an all-solid beachball.

tern. Therefore, under the assumption of a 1-D Earth model, the recorded transverse-component surface waves will be Love waves, and they could be used to discriminate between a force and moment tensor, as long as the true source was not a perfectly vertical force or a pure explosion or implosion. Furthermore, good station coverage and good waveform signal-to-noise would be needed.

With the observed Love waves (Fig. 2), critical question remains: did they arise from a source process or a wave propagation effect related to topography, bathymetry, and 3-D wave speed heterogeneities? 3-D wavefield simulations demonstrate that these effects can strongly influence the wavefield, implying that if they are not taken into account during the forward modelling, the estimated source model could be negatively impacted. For example, Burgos *et al.* (2016) focused on heterogeneities surrounding the source and concluded that 'the difference between the effective and real moment tensors could be large in the presence of local heterogeneities, which should not be neglected given that the inverse problem only gives access to the effective tensor' (p. 4385). The studies of Takemura *et al.* (2015) and Gualtieri *et al.* (2020) considered the influences of topography, bathymetry, and realistic wave speed heterogeneities at local and global scales, respectively. Realistically, there are likely influences from both source and structure on the generation of Love waves, including with the case of the HTHH event. Future work is needed to address the influences of Earth structure.

7 CONCLUSIONS

We consider two highly simplified point-source models—force and moment tensor—for the main ∼270 s seismic signal of the HTHH volcanic eruption. Our emphasis is on comprehensively searching the model parameter space. Considering only the first subevent, we are able to perform a complete grid search of model parameter space,

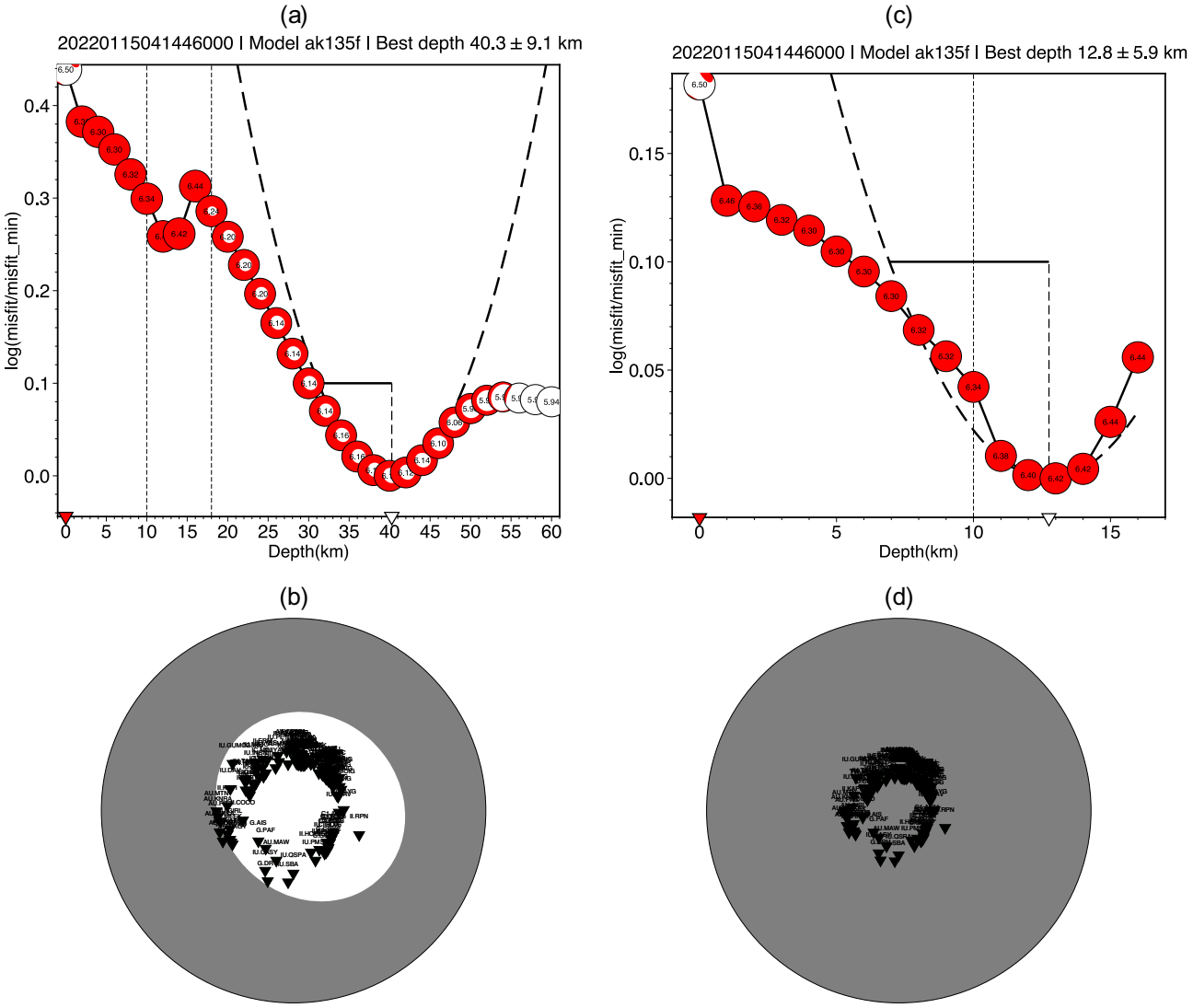

Figure 16. The impact of cycle-skipping on estimating source parameters, illustrated for fitting teleseismic *P* waveforms with a moment tensor. Both depth and magnitude are free parameters, as is the moment tensor orientation (three parameters) and source type (lune longitude and lune latitude). These are Runs SM1 and SM1-X (Table 2). (a) Waveform misfit versus depth over the depth range 0–30 km. For each depth, the best-fitting moment tensor is plotted as a beachball, with its magnitude labeled. (b) Best-fitting moment tensor from (a), which occurs for a depth of 40 km. The station symbols represent the lower-hemisphere piercing points of the ray paths to each station, assuming the 1-D Earth model AK135f. (c) and (d) Same as (a) and (b), but for the depth range 0–16 km. Over this range, the best-fitting moment tensor has all-positive eigenvalues and is coloured solid. See Section 6.3 for details.

Table 4. Best set of force parameters (Table 3) for subevents S1–S4, among the 10 realizations in Fig. 10. The sum of all forces is $(1.7 \pm 0.1) \times 10^{14}$ N. A text file containing higher-precision values is provided in the Supporting Information.

Parameter	t_i (s)	$t_i - t_1$ (s)	$\|\mathbf{f}\|$ (N)	θ	ϕ
S1	50.85	0	6.95×10^{13}	158°	139°
S2	256.09	205.23	4.75×10^{13}	169°	142°
S3	293.51	242.66	3.94×10^{13}	163°	160°
S4	321.12	270.27	3.16×10^{13}	179°	6°

with 1.9×10^9 evaluations of a waveform misfit function. Considering all subevents simultaneously, as well as their onset times, we shifted to CMA-ES to efficiently search spaces of up to 28 model parameters.

We summarize our findings based on the single subevent analysis as follows:

(i) The lack of a clear high-frequency signal for the main subevent poses challenges for estimating the origin time and, in turn, for determining the proper alignment of synthetic and observed waveforms, both for *P* and surface waves.

(ii) We determined a new origin time, 2022-01-15 04:15:19.6 ±1.7 s, which is 34.6 s later than the origin time reported by USGS,

Table 5. Best set of moment tensor parameters (Table 3) for subevents S1–S4, among the 10 realizations in Fig. 12. The cumulative magnitude is M_w 6.5. A text file containing higher-precision values is provided in the Supporting Information.

Parameter	t_i (s)	$t_i - t_1$ (s)	m_i	γ	δ	κ	σ	θ
S1	50.88	0	6.11	−28°	68°	109°	65°	58°
S2	256.47	205.59	6.33	−29°	65°	136°	83°	52°
S3	294.30	243.42	6.00	−30°	66°	124°	60°	53°
S4	320.47	269.59	6.06	−22°	61°	62°	90°	66°

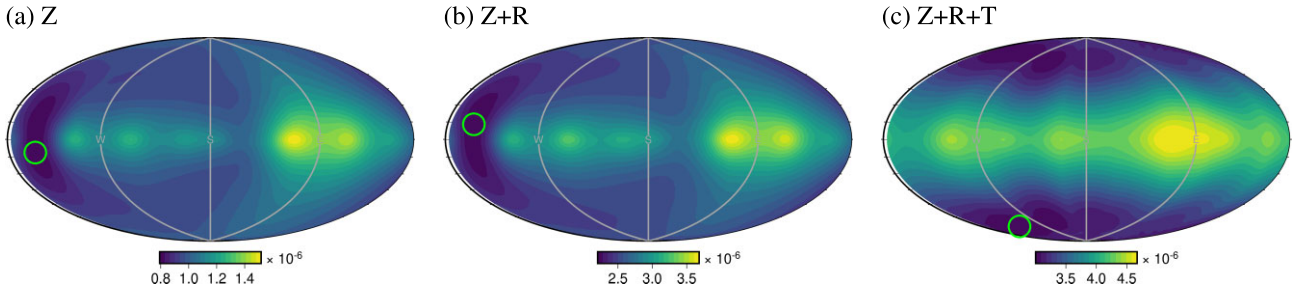

Figure 17. The impact of waveform components (Z, R, T) on estimating source parameters using regional surface wave data. Here, the source model is a point force (direction and amplitude), and the depth is assumed to be fixed at 1 km. The corresponding results for unfixed depth can be found in Thurin & Tape (2023). (a) Surface waveform misfit as a function of force direction, using vertical-component data only (Run SF6 of Table 2). (b) Same as (a), but using vertical and radial components (Run SF7 of Table 2). (c) Same as (a), but using vertical, radial and transverse components (Run SF8 of Table 2). The inclusion of the transverse component leads to a best-fitting point force that points downward ($\theta = 156°$) instead of horizontally (99° in a, 79° in b).

based on the average P-wave time-shifts over 142 stations for the best-fitting point force and moment tensor, respectively, at a depth of 1 km.

(iii) End-member sources—upward force, downward force, explosion moment tensor, and implosion moment tensor—can provide synthetic waveforms that reasonably fit observed waveforms (Fig. 3), under the assumption that synthetics can be time-shifted to account for unknown Earth structure relative to the assumed 1-D Earth model.

(iv) Exploration of model parameter space—even for the simple source models considered here—provides a complex view of misfit function variations and trade-offs among model parameters such as source amplitude, orientation and depth.

(v) The tangential component Love waves (e.g. Figs 2 and 7) are essential for estimating the best-fitting force direction (Fig. 17).

(vi) We formally estimated the tilt of the source models, which is of the order of 30°. This deflection from vertical is necessary for the point-source model to generate Love waves, while not necessary for explosive-like moment tensor sources (so long as they have $\lambda_2 \neq \lambda_3$, Rösler & van der Lee 2020). Nonetheless, both source models share the same general orientation, which is consistent with what is discussed by Garza-Girón *et al.* (2023) and Zheng *et al.* (2023). (Even though Zheng et al. 2023 interpreted an upward force, they found that a 25° tilt was adequate to explain the transverse signal.)

(vii) The best-fitting depth differs for the choice of source model and waveforms: 28 km for force and P waves (SF1), 11 km for force and surface waves (SF2), 13 km for moment tensor and P waves (SM1-X), and 1 km for moment tensor and surface waves. The set of fixed-depth runs at 1 km supports other evidence that the source of the seismic signal was shallow.

(viii) A downward-pointing source provides better waveform fits than an upward-pointing source (Fig. 3, also shown in Thurin & Tape 2023, SF9-SF12). An explosion-like moment tensor provides better waveform fits than an implosion-like moment tensor (Fig. 3, also shown in Thurin & Tape 2023, SM9-SM12).

(ix) From the fixed-depth runs, the magnitude of the best-fitting moment tensor is larger (SM5: M_w 6.46) for body waves than for surface waves (SM8: M_w 6.16), while the amplitude of the best-fitting force is similar for body waves (SF5: 0.85×10^{14} N) and surface waves (0.71×10^{14} N). Further study is needed to consider body waves and surface waves simultaneously within the inversion, and ideally, this would be done in conjunction with consideration of bathymetry, topography, and realistic 3-D wave speed heterogeneities (Section 6.4).

We summarize our findings based on the multi-subevent analysis as follows:

(i) We were able to leverage the efficiency of the CMA-ES algorithm to perform a joint search of up to 28 model parameters.

(ii) The cumulative amplitude of the sequence of four point-force subevents is $(1.7 \pm 0.1) \times 10^{14}$ N. The cumulative moment magnitude for the sequence of four moment tensor subevents is M_w 6.5 ± 0.03.

(iii) The similarity of the four subevent source models—both force and moment tensor—suggests that a repeating source hypothesis is reasonable. (This hypothesis was used in the case of the four subevent moment tensors in Thurin *et al.* 2022.)

(iv) The inversion over point-force subevents yields a sequence of sub-vertical forces of decreasing amplitude (Fig. 11b). By comparison, the magnitudes of the subevent moment tensors did not necessarily decrease with onset time (Fig. 13b).

(v) Multi-subevent inversions face the same challenges of cycle-skipping as in the single-subevent inversions, and this is especially true in the case of the force source (Fig. 11d versus Fig. 13d).

This study illustrates the complexity of a large misfit space for a series of subevents, especially when dealing with overlapping signals in the period range of interest. The events are well-separated in time in the high-frequency teleseismic stacks, but when filtered

at 25–70 s, subevents S2–S4 overlap significantly, which motivated our joint inversion of their source parameters. The relative timing measured from the body waves provided critical information, as it allowed us to perform path calibration before estimating the sequence.

A limitation of this seismic study is the simplistic 1-D Earth model used to solve our forward problem, especially within a complex subduction setting. One approach would be to adopt variations in 1-D Earth models (Phạm & Tkalčić 2021) or consider alternative misfit functions that mitigate the effects of an imperfect 1-D model (Scarinci *et al.* 2023); another approach would be to use 3-D Earth models, including topography and bathymetry (Liu *et al.* 2004). A 3-D Earth model would potentially reduce the ambiguity with respect to source magnitudes by accounting for local structures and near-source heterogeneities, thereby producing more accurate regional surface waves (Section 6.4). However, the quality of any 3-D Earth model in the region of interest will be limited by the sparse data coverage. Therefore, rather than considering 3-D synthetic seismograms, we have turned toward the comprehensive exploration of model parameter space, enabled by the CMA-ES method.

ACKNOWLEDGMENTS

We thank editors Rudolf Widmer-Schnidrig and Ducan Agnew, as well as two anonymous reviewers, for providing critical and constructive feedback that led us toward a more comprehensive study. We thank University of Alaska Fairbanks (UAF) Research Computing Systems for an allocation on the 'chinook' high-performance computing cluster. We benefited from helpful discussions with colleagues at University of Alaska, University of Toronto, University of South Florida, and Ryan Modrak. This project was supported by Air Force Research Laboratory contract HQ0034-20-F-0284, funded through the UAF Geophysical Detection of Nuclear Proliferation (GDNP) University Affiliated Research Center (UARC).

DATA AVAILABILITY

(i) Supporting results for the 25 single-subevent runs discussed in Section 4 are provided in the collection of Thurin & Tape (2023).

(ii) Supporting results for the multi-subevent runs discussed in Section 5 are provided as YouTube playlists at https://www.youtube.com/playlist?list=PLp-dlSTG4TvHXizV_IIGy1GgNsAUgJEvr (force: Fig. 10) and https://www.youtube.com/playlist?list=PLp-dlSTG4TvHToQl39kNW8gj0uSFGA_3q (moment tensor: Fig. 12). Each playlist includes 10 runs each and demonstrates the variability of randomly seeded searches of model parameter space.

(iii) Seismic data were obtained from the Incorporated Research Institutions for Seismology Data Management Center (IRIS DMC). We use stations from the Geoscope network (G, https://doi.org/10.18715/GEOSCOPE.G), the Global Seismograph Network (II, https://doi.org/10.7914/SN/II and IU https://doi.org/10.7914/SN/IU), the Australian National Seismograph Network (AU, https://doi.org/10.26186/144675) and the New Zealand National Seismograph Network (NZ, https://doi.org/10.21420/G19Y-9D40).

(iv) The moment tensor code used in this study, MTUQ, is openly available at https://github.com/uafgeotools/mtuq.

(v) The Obspy code (Beyreuther *et al.* 2010; Krischer *et al.* 2015) is available at https://github.com/obspy/obspy

(vi) The GCMT catalogue (Dziewonski *et al.* 1981; Ekström *et al.* 2012) is accessible via https://www.globalcmt.org/

(vii) The USGS NEIC catalog origin time of 2022-01-15 04:14:45 UTC and magnitude of M_w 5.8 were obtained from https://earthquake.usgs.gov/earthquakes/eventpage/us7000gc8r (last accessed 2023 April).

REFERENCES

Alvizuri, C., Silwal, V., Krischer, L. & Tape, C., 2018. Estimation of full moment tensors, including uncertainties, for nuclear explosions, volcanic events, and earthquakes, *J. geophys. Res. Solid Earth,* **123,** 5099–5119.

Alvizuri, C. & Tape, C., 2016. Full moment tensors for small events (M_w < 3) at Uturuncu volcano, Bolivia, *Geophys. J. Int.,* **206,** 1761–1783.

Alvizuri, C. & Tape, C., 2018. Full moment tensor analysis of nuclear explosions in North Korea, *Seismol. Res. Lett.,* **89**(6), 2139–2151.

Amores, A., Monserrat, S., Marcos, M., Arüeso, D., Villaonga, J., Jordá, G. & Gomis, D., 2022. Numerical simulation of atmospheric Lamb waves generated by the 2022 Hunga-Tonga volcanic eruption, *Geophys. Res. Lett.,* **49,** 1–8.

Beyreuther, M., Barsch, R., Krischer, L.,Megies, T., Behr, Y. & Wassermann, J., 2010. ObsPy: A Python Toolbox for Seismology, *Seismological Research Letters,* **81**(3), 530–533.

Biedrzycki, R., 2020. Handling bound constraints in CMA-ES: an experimental study, *Swarm Evolution. Comput.,* **52,** 1–15.

Bird, P., 2003. An updated digital model of plate boundaries, *Geochem. Geophy. Geosyst.,* **4,** 1–52.

Burger, R.W. & Langston, C.A., 1985. Source mechanism of the May 18, 1980, Mount St. Helens eruption from regional surface waves, *J. geophys. Res.,* **90**(B9), 7653–7664.

Burgos, G., Capdeville, Y. & Guillot, L., 2016. Homogenized moment tensor and the effect of near-field heterogeneities on nonisotropic radiation in nuclear explosion, *J. geophys. Res. Solid Earth,* **121,** 4366–4389.

Carr, J.L., Horváth, A., Wu, D.L. & Friberg, M.D., 2022. Stereo plume height and motion retrievals for the record-setting Hunga Tonga-Hunga Ha'apai eruption of 15 January 2022, *Geophys. Res. Lett.,* **49,** 1–7.

Chiang, A., Dreger, D.S., Ford, S.R. & Walter, W.R., 2014. Source characterization of underground explosions from combined regional moment tensor and first-motion analysis, *Bull. seism. Soc. Am.,* **104**(4), 1587–1600.

Chiang, A., Dreger, D.S., Ford, S.R., Walter, W.R. & Yoo, S.-H., 2016. Moment tensor analysis of very shallow sources, *Bull. seism. Soc. Am.,* **106**(6), 2436–2449.

Chouet, B. *et al.*, 2003. Source mechanisms of explosions at Stromboli Volcano, Italy, determined from moment-tensor inversions of very-long-period data, *J. geophys. Res.,* **108**(B1), doi:10.1029/2002JB001919.

Chouet, B.A., 1996. New methods and future trends in seismological volcano monitoring, in *Monitoring and Mitigation of Volcano Hazards,* pp. 23–97, eds Scarpa, R. & Tilling, R.I., Springer, Berlin.

Dalcin, L. & Fang, Y.-L.L., 2021. mpi4py: Status update after 12 years of development, *Comput. Sci. Eng.,* **23**(4), 47–54.

Day, S.M. & McLaughlin, K.M., 1991. Seismic source representations for spall, *Bull. seism. Soc. Am.,* **81**(1), 191–201.

Dziewonski, A., Chou, T.-A. & Woodhouse, J.H., 1981. Determination of earthquake source parameters from waveform data for studies of global and regional seismicity, *J. geophys. Res.,* **86**(B4), 2825–2852.

Ekström, G., Nettles, M. & Dziewoński, A.M., 2012. The global GCMT project 2004–2010: centroid-moment tensors for 13,017 earthquakes, *Phys. Earth planet. Inter.,,* **200-201,** 1–9.

Ford, S.R., Dreger, D.S. & Walter, W.R., 2010. Network sensitivity solutions for regional moment-tensor inversions, *Bull. seism. Soc. Am.,* **100**(5A), 1962–1970.

Ford, S.R., Walter, W.R. & Dreger, D.S., 2012. Event discrimination using regional moment tensors with teleseismic-*P* constraints, *Bull. seism. Soc. Am.,* **102**(2), 867–872.

Garza-Girón, R., Lay, T., Pollitz, F., Kanamori, H. & Rivera, L., 2023. Solid Earth–atmosphere interaction forces during the 15 January 2022 Tonga eruption, *Sci. Adv.,* **9,** 1–11.

Gualtieri, L., Bachmann, E., Simons, F.J. & Tromp, J., 2020. The origin of secondary microseism Love waves, *Proc. Natl. Acad. Sci.,* **117**(47), 29504–29511.

Hansen, N., 2016. *The CMA evolution strategy: a tutorial,* https://arxiv.org/abs/1604.00772.

Hansen, N., Arnold, D.V. & Auger, A., 2015. Evolution strategies, in *Springer Handbook of Computational Intelligence,* Springer, pp. 871–898, eds Kacprzyk, J. & Pedrycz, W., Berlin.

Hansen, N., Auger, A., Ros, R., Mersmann, O., Tušar, T. & Brockhoff, D., 2021. COCO: a platform for comparing continuous optimizers in a black-box setting, *Optimiz. Methods Softw.,* **36**(1), 114–144.

Hansen, N. & Ostermeier, A., 2001. Completely derandomized self-adaptation in evolution strategies, *Evolution. Comput.,* **9**(2), 159–195.

Jarrard, R.D., 1986. Relations among subduction parameters, *Rev. Geophys.,* **24**(2), 217–284.

Jarrard, R.D., 2003. Subduction fluxes of water, carbon dioxide, chlorine, and potassium, *Geochem. Geophy. Geosyst.,* **4**(5), doi:10.1029/2002GC000392.

Kanamori, H. & Given, J.W., 1982. Analysis of long-period seismic waves excited by the May 18, 1980, eruption of Mount St.Helens—a terrestrial monopole?, *J. geophys. Res.,* **87**(B7), 5422–5432.

Kanamori, H., Given, J.W. & Lay, T., 1984. Analysi of seismic body waves excited by the Mount St. Helens eruption of May 18, 1980, *J. geophys. Res.,* **89**(B3), 1856–186.

Krause, O., Arbonès, D. & Igel, C., 2016. CMA-ES with Optimal Covariance Update and Storage Complexity, eds Lee, D., Sugiyama, M., Luxburg, U., Guyon, I. & Garnett, R., *Advances in Neural Information Processing Systems,* **29,** Curran Associates, Inc., 370–378.

Krischer, L., Hutko, A.R., van Driel, M., Stähler, S., Bahavar, M., Trabant, C. & Nissen-Meyer, T., 2017. On-demand custom broadband synthetic seismograms, *Seismol. Res. Lett.,* **88**(4), 1127–1140.

Krischer, L., Megies, T., Barsch, R., Beyreuther, M., Lecocq, T., Caudron, C. & Wassermann, J., 2015. ObsPy: A bridge for seismology into the scientific Python ecosystem., *Computational Science & Discovery,* **8**(1), 014003.

Legrand, D., Kaneshima, S. & Kawakatsu, H., 2000. Moment tensor analysis of near-field broadband waveforms observed at Aso Volcano, Japan, *J. Volc. Geotherm. Res.,* **101,** 155–169.

Liu, Q., Polet, J., Komatitsch, D. & Tromp, J., 2004. Spectral-element moment tensor inversions for earthquakes in southern California, *Bull. seism. Soc. Am.,* **94**(5), 1748–1761.

Matoza, R.S. *et al.*, 2022. Atmospheric waves and global seismoacoustic observations of the January 2022 Hunga eruption, Tonga, *Science,* **377,** 95–100.

Montagner, J.-P. & Kennett, B. L.N., 1996. How to reconcile body-wave and normal-mode reference earth models, *Geophys. J. Int.,* **125,** 229–248.

Nishimura, T. & Hamaguchi, H., 1993. Scaling law of volcanic explosion earthquake, *Geophys. Res. Lett.,* **20**(22), 2479–2482.

Nissen-Meyer, T., van Driel, M., Stähler, S.C., Hosseini, K., Hempel, S., Auer, L., Colombi, A. & Fournier, A., 2014. AxiSEM: broadband 3-D seismic wavefields in axisymmetric media, *Solid Earth,* **5,** 425–445.

Ohminato, T., Takeo, M., Kumagai, H., Yamashina, T., Oikawa, J., Koyama, E., Tsuji, H. & Urabe, T., 2006. Vulcanian eruptions with dominant single force components observed during the Asama 2004 volcanic activity in Japan, *Earth Planets Space,,* **58,** 583–593.

Omira, R., Ramalho, R.S., Kim, J., González, P.J., Kadri, U., Miranda, J.M., Carrilho, F. & Baptista, M.A., 2022. Global Tonga tsunami explained by a fast-moving atmospheric source, *Nature,* **609,** 734–740.

Pakoksung, K., Supparsi, A. & Imamura, F., 2022. The near-field tsunami generated by the 15 January 2022 eruption of the Hunga Tonga-Hunga Ha'apai volcano and its impact on Tongatapu, Tonga, *Sci. Rep.,* **12,** 1–15.

Phạm, T.-S. & Tkalčić, H., 2021. Toward improving point-source moment-tensor inference by incorporating 1D Earth model's uncertainty: implications for the Long Valley Caldera earthquakes, *J. geophys. Res. Solid Earth,* **126,** 1–27.

Poli, P. & Shapiro, N.M., 2022. Rapid characterization of large volcanic eruptions: measuring the impulse of the Hunga Tonga Ha'apai explosion from teleseismic waves, *Geophys. Res. Lett.,* **49,** 1–9.

Pošík, P., Huyer, W. & Pál, L., 2012. A comparison of global search algorithms for continuous black box optimization, *Evolution. Comput.,* **20**(4), 509–541.

Proud, S.R., Prata, A.T. & Schmauß, S., 2022. The January 2022 eruption of Hunga Tonga-Hunga Ha'apai volcano reached the mesosphere, *Science,* **378,** 554–557.

Rösler, B. & van der Lee, S., 2020. Using seismic source parameters to model frequency-dependent surface-wave radiation patterns, *Seismol. Res. Lett.,* **91**(2A), 992–1002.

Scarinci, A., bin Waheed, U., Gu, C., Ren, X., Dia, B.M., Kaka, S., Fehler, M. & Marzouk, Y., 2023. Robust Bayesian moment tensor inversion with optimal transport misfits: layered medium approximations to the 3-D SEG-EAGE overthrust velocity model, *Geophys. J. Int.,* **234,** 1169–1190.

Shi, Q., Wei, S. & Chen, M., 2018. An MCMC multiple point sources inversion scheme and its application to the 2016 Kumamoto M_w6.2 earthquake, *Geophys. J. Int.,* **215,** 737–752.

Simons, F.J., Simon, J.D. & Pipatprathanporn, S., 2021. Twenty-thousand leagues under the sea: recording earthquakes with autonomous floats, *Acoust. Today,* **17**(2), 42–51.

Suttorp, T., Hansen, N. & Igel, C., 2009. Efficient covariance matrix update for variable metric evolution strategies, *Mach. Learn.,* **75**(2), 167–197.

Takemura, S., Furumura, T. & Maeda, T., 2015. Scattering of high-frequency seismic waves caused by irregular surface topography and small-scale velocity inhomogeneity, *Geophys. J. Int.,* **201,** 459–474.

Takeo, M., 1990. Analysis of long-period seismic waves excited by the November 1987 eruption of Izu-Oshima volcano, *J. geophys. Res.,* **95**(B12), 19377–19393.

Tameguri, T., Iguchi, M. & Ishihara, K., 2002. Mechanism of explosive eruptions from moment tensor analyses of explosion earthquakes at Sakurajima volcano, Japan, *Bull. Volc. Soc. Japan,* **47**(4), 197–215.

Tape, W. & Tape, C., 2012. A geometric setting for moment tensors, *Geophys. J. Int.,* **190,** 476–498.

Tarumi, K. & Yoshizawa, K., 2023. Eruption sequence of the 2022 Hunga Tonga-Hunga Ha'apai explosion from back-projection of teleseismic P waves, *Earth planet. Sci. Lett.,* **603,** 1–9.

Thurin, J. & Tape, C., 2023. *Estimation of best-fitting force, moment tensor, and depth for the 2022 Hunga-Tonga submarine volcanic eruption,* Version 1.0 [Data set]. Zenodo, doi:10.5281/zenodo.7811955.

Thurin, J., Tape, C. & Modrak, R., 2022. Multi-event explosive seismic source for the 2022 M_w6.3 Hunga Tonga submarine volcanic eruption, *Seismic Record,* **2**(4), 217–226.

Uhira, K. & Takeo, M., 1994. The source of explosive eruptions of Sakurajima volcano, Japan, *J. geophys. Res.,* **99**(B9), 17775–17789.

van Driel, M., Krischer, L., Stähler, S.C., Hosseini, K.& Nissen-Meyer, T. , 2015. Instaseis: instant global seismograms based on a broadband waveform database, *Solid Earth,* **6,** 701–717.

Vömel, H., Evan, S. & Tully, M., 2022. Water vapor injection into the stratosphere by Hunga Tonga-Hunga Ha'apai, *Science,* **377,** 1444–1447.

Walter, W.R. & Wen, L., 2018. Preface to the focus section on North Korea's September 2017 nuclear test and its aftermath, *Seismol. Res. Lett.,* **89**(6), 2013–2016.

Yuen, D.A. *et al.*, 2022. Under the surface: pressure-induced planetary-scale waves, volcanic lightning, and gaseous clouds caused by the submarine eruption of Hunga Tonga-Hunga Ha'apai volcano, *Earthq. Res. Adv.,* **2,** 1–13.

Zheng, Y. *et al.*, 2023. Episodic magma hammers for the 15 january 2022 cataclysmic eruption of hunga tonga-hunga ha'apai, *Geophys. Res. Lett.,* **50**(8), e2023GL102763, doi:10.1029/2023GL102763.

Zhu, L. & Helmberger, D., 1996. Advancement in source estimation techniques using broadband regional seismograms, *Bull. seism. Soc. Am.,* **86**(5), 1634–1641.

SUPPORTING INFORMATION

Supplementary data are available at *GJI* online.

Figure S1. Surface waveforms fits for two trial sources: downward force (Run SF12) and isotropic explosion (Run SM12). A grid search is performed to find the (a) best-fitting force amplitude and (b) magnitude. Neither of these sources generates transverse-component synthetic seismograms when using a 1-D Earth model. See Thurin & Tape (2023) for expanded details.
Figure S2. Surface waveforms fits for two trial sources: upward force (Run SF11) and isotropic implosion (Run SM11). A grid search is performed to find the (a) best-fitting force amplitude and (b) magnitude. Neither of these sources generates transverse-component synthetic seismograms when using a 1D Earth model. See Thurin & Tape (2023) for expanded details.
Figure S3. Regional surface waves used to estimate a multi-event source model using the CMA-ES method. Observed data are in black, synthetics are in red. Seismograms are filtered 25–70 s and displayed for vertical (left), radial (middle), and transverse (right) components. The source model used here is a moment tensor, which differs for each subevent. Depth is fixed to 1 km. (a) Waveforms (red) for one of the CMA-ES initialization (four sources at random). (b) Waveforms (red) for the final iteration of the best-fitting run (Fig. 11a). All waveform time-windows include the data considered for the inversion, and is therefore relative timing (650 s time-window) centred on the surface waves signals. The lowermost panels shows the source time function of (a) and (b), with respect to the USGS origin time.

Please note: Oxford University Press is not responsible for the content or functionality of any supporting materials supplied by the authors. Any queries (other than missing material) should be directed to the corresponding author for the paper.

APPENDIX A: COVARIANCE MATRIX ADAPTATION EVOLUTION STRATEGY

The CMA-ES introduced by Hansen & Ostermeier (2001) is a gradient-free (black-box) iterative optimization method that performs efficiently on a variety of non-smooth, non-convex, and multimodal misfit spaces (Suttorp *et al.* 2009). Its goal is to provide a candidate solution that minimizes a misfit function $f : R^n \rightarrow R$. It is well suited for inverse problems for which gradients are not readily available and on problems ranging from a few to a few hundred parameters. Its main peculiarity lies in its combined use of covariance adaptation, which controls the orientation of the sampling distribution, and cumulative step length adaptation, which controls the step size. The term *cumulation* refers to the 'memory' capacity of CMA-ES, as it gathers and uses information during the search from previous iterations (as opposed to using only the current state). It also benefits from interesting properties such as scale and rotation invariances, and 'quasi-Newton-like' behaviour on convex-quadratic objective functions.

At each generation g, the CMA-ES algorithm evaluates λ candidate solutions, randomly sampled from a multivariate Gaussian distribution $\mathcal{N}(\mathbf{m}, \mathbf{C})$, uniquely defined by its mean $\mathbf{m} \in R^n$ and covariance matrix $\mathcal{C} \in R^{n\times n}$, following

$$\mathbf{x}_k^{g+1} \sim \mathbf{m}^g + \sigma^g \mathcal{N}(0, \mathbf{C}^g) \quad \text{with} \quad k = 1, \ldots, \lambda, \tag{A1}$$

where $\mathbf{x}_k^{g+1}$ is the kth offspring (candidate solution) of the next generation, drawn from the current distribution $\mathcal{N}(\mathbf{m}^g, \mathbf{C}^g)$, and σ^g is the CMA-ES overall variance that controls the step size of the search. Each offspring's fitness is evaluated, and they are ranked such that

$$f\left(\mathbf{x}_{1:\lambda}^{g+1}\right) \leq f\left(\mathbf{x}_{2:\lambda}^{g+1}\right) \leq \ldots \leq f\left(\mathbf{x}_{\lambda:\lambda}^{g+1}\right), \tag{A2}$$

with i: λ denoting the ith best-fitting offspring. The mean is then updated by a recombination of the μ (typically $\mu = \lambda/2$) best offspring such that

$$\mathbf{m}^{g+1} = \sum_{i=1}^{\mu} \mathbf{x}_{i:\lambda}^{g+1} w_i, \tag{A3}$$

where w_i are the positive weights coefficients for the weighted mean computation, satisfying $w_1 \geq w_2 \geq \ldots \geq w_\mu$ and $\sum_{i=1}^{\mu} w_i = 1$. The mean update is directly controlled by the best-fitting samples, which in turn ensure convergence toward the lower misfit regions. Following the same principle, the global step size σ^g and the covariance matrix $\mathbf{C}$ are also updated, given the performances of the candidate distribution. The covariance matrix is updated in two steps.

(i) First, we consider a rank-1 update accounting for the changes of $\mathbf{m}$ over time (the global trajectory of the distribution within the misfit space), which is based on an evolution path $\mathbf{p}_c$ given by

$$\mathbf{p}_c^{g+1} = (1 - c_c)\mathbf{p}_c^g + \sqrt{c_c(2 - c_c)\mu_{eff}}\, \frac{\mathbf{m}^{g+1} - \mathbf{m}^g}{\sigma^g}, \tag{A4}$$

where $c_c \in [0, 1]$ is a discount factor controlling the cumulation time of the path length $\mathbf{p}_c$ and $\mu_{\text{eff}} = \sum_{i=1}^{\mu} w_i^2$ is the effective sample size given the weights. The path length $\mathbf{p}_c$ encapsulates a long-term average of the mean update: it becomes large when successive steps in the same direction are taken and small when they take alternate directions from generation to generation (Krause *et al.* 2016).

(ii) Subsequently, we examine a rank-μ update, which promotes the μ successful offsprings by transforming $\mathbf{C}$ to align with their empirical covariance.

Combining rank-1 and rank-μ yields

$$\mathbf{C}^{g+1} = (1 - c_1 - c_\mu)\mathbf{C}^g + c_1 \mathbf{p}_c^g \mathbf{p}_c^{g\,T} + c_\mu \sum_{i=1}^{\mu} w_i \left(\frac{\mathbf{x}_{i:\lambda}^g - \mathbf{x}^g}{\sigma^g}\right)\left(\frac{\mathbf{x}_{i:\lambda}^g - \mathbf{x}^g}{\sigma^g}\right)^T, \tag{A5}$$

where the terms c_1 and c_μ are the learning rate for rank-1 and rank-μ updates.

The global step-size update is also controlled by a path length term, $\mathbf{p}_\sigma$,

$$\mathbf{p}_\sigma^{g+1} = (1 - c_\sigma)\mathbf{p}_\sigma^g + \sqrt{c_\sigma(2 - c_\sigma)}\sqrt{\mu_{\text{eff}}}(\mathbf{C}^g)^{-1/2}\frac{\mathbf{m}^{g+1} - \mathbf{m}^g}{\sigma^g}, \tag{A6}$$

where $c_\sigma \in [0, 1]$ is a discount factor controlling the cumulation time of $\mathbf{p}_\sigma$. $\mathbf{p}_\sigma^{g+1}$ accounts for the path of $\mathbf{m}$ in an isotropic space (normalization by $\mathbf{C}^{1/2}$), tracking the correlation of successive generations, which is simplified in a normalized coordinate system. Finally, σ^g is updated following

$$\sigma^{g+1} = \sigma^g \times \exp\left(\frac{c_\sigma}{d_\sigma}\left(\frac{\|\mathbf{p}_\sigma^{g+1}\|}{E\|\mathcal{N}(0, \mathbf{I_n})\|} - 1\right)\right), \tag{A7}$$

with $E\|\mathcal{N}(0, \mathbf{I_n})\|$ is the expected length of a purely random path and d_σ a damping factor. The cumulative step length adaptation is

essentially comparing the path length $\mathbf{p}_{\sigma}^{g+1}$ to a random length and increases or decreases the step size to balance the correlation of successive generations. The successive covariance and step-size adaptation, combined with the recombination (sorted weighted mean), result in a very powerful optimization scheme, that has outperformed a vast majority of other black-box methods on standardized benchmarks (Pošík *et al.* 2012; Hansen *et al.* 2021).

Our CMA-ES implementation includes the boundary handling methods of Biedrzycki (2020), which are particularly useful for the parameters we are inverting, most of which exist within bounded domains.

When new samples are drawn using eq. (A1), we apply the 'Rand-based' method to repair any samples that fall outside the valid bounds. This method re-projects the values within the bounds at random, redrawing uniformly between the violated bound and the current parameter mean. This ensures that all samples remain within the valid parameter space. For the angular values defined within a periodic domain, such as the strike angle κ and force azimuthal angle ϕ, which are defined between [0, 360] deg, we apply the 'wrapping' method, which re-projects the sample within the bounds, using circular periodicity to ensure that the values remain within the valid range.